Journal Pre-proof

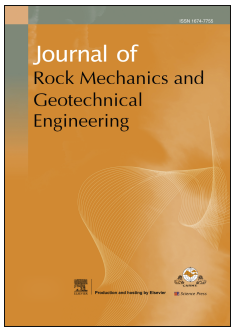

Multiscale monitoring and analysis of complex rupture and source mechanisms of mining-related seismicity on fault networks

Chunhui Song, Caiping Lu, Xiufeng Zhang, T.C. Sunilkumar, Derek Elsworth, Jiefang Song, Chengyu Liu, Yang Liu

PII: S1674-7755(24)00526-2

DOI: https://doi.org/10.1016/j.jrmge.2024.11.015

Reference: JRMGE 1821

To appear in: *Journal of Rock Mechanics and Geotechnical Engineering*

Received Date: 18 June 2024

Revised Date: 31 October 2024

Accepted Date: 7 November 2024

Please cite this article as: Song C, Lu C, Zhang X, Sunilkumar TC, Elsworth D, Song J, Liu C, Liu Y, Multiscale monitoring and analysis of complex rupture and source mechanisms of mining-related seismicity on fault networks, *Journal of Rock Mechanics and Geotechnical Engineering*, https://doi.org/10.1016/j.jrmge.2024.11.015.

Multiscale monitoring and analysis of complex rupture and source mechanisms of mining-related seismicity on fault networks

Chunhui Song [a], Caiping Lu [a, *], Xiufeng Zhang [b], T.C. Sunilkumar [c], Derek Elsworth [d], Jiefang Song [a], Chengyu Liu [e], Yang Liu [a]

[a] Key Laboratory of Deep Coal Resource Mining (Ministry of Education), School of Mines, China University of Mining and Technology, Xuzhou, 221116, China

[b] Center of Rockburst Prevention Research, Shandong Energy Group, Jinan, 250101, China

[c] Department of Earth and Space Sciences, Southern University of Science and Technology, Guangdong, 518055, China

[d] Department of Energy and Mineral Engineering, EMS Energy Institute and G3 Center, Pennsylvania State University, University Park, PA, 16802, USA

[e] Shandong Earthquake Agency, China Earthquake Administration, Jinan, 250014, China

[*] Corresponding author. E-mail address: cplucumt@126.com (C.P. Lu).

Abstract: Mining-related seismicity poses significant challenges in underground coal mining due to its complex rupture mechanisms and associated hazards. To bridge gaps in understanding these intricate processes, this study employed a multi-local seismic monitoring network, integrating both in-mine and local instruments at overlapping length scales. We specifically focused on a damaging local magnitude (M_L) 2.6 event and its aftershocks that occurred on 10 September 2022 in the vicinity of the 3308 working face of the Yangcheng coal mine in Shandong Province, China. Moment tensor (MT) inversion revealed a complex cascading rupture mechanism: an initial moment magnitude (M_w) 2.2 normal fault slip along the DF60 fault in an ESE–WNW direction, transitioning to a M_w 3.0 event as the FD24 and DF60 faults unclamped. The scale-independent self-similarity and stress heterogeneity of mining-related seismicity were investigated through source parameter calculations, providing valuable insights into the driving mechanism of these seismic sequences. The in-mine network, constrained by its low dynamic changes, captured only the nucleation phase of the DF60 fault. Furthermore, standard decomposition of the MT solution from the seismic network proved inadequate for accurately identifying the complex nature of the rupture. To enhance safety and risk management in mining environments, we examined the implications of source reactivation within the cluster area post-stress-adjustment. This comprehensive multiscale analysis offers crucial insights into the complex rupture mechanisms and hazards associated with mining-related seismicity. The results underscore the importance of continuous multi-local network monitoring and advanced analytical techniques for improved disaster assessment and risk mitigation in mining operations.

Keywords: Mining-Induced seismicity; Mining-triggered seismicity; Complex rupture; Collapse model; Multiscale monitoring

1. Introduction

The underground mining environment presents unique challenges in the occurrence of seismic events, which pose significant risks to worker safety, infrastructure integrity, and overall productivity. Unlike natural tectonic earthquakes, mining-related seismicity results from human activities altering stress conditions around the mine (Cesca et al., 2013; Dahm et al., 2013). Although these events generally have lower magnitudes, their proximity to underground voids can amplify seismic waves, heightening the risk of disasters (Paap et al., 2018; Song et al., 2024). Mining-related seismicity is typically categorised into two main types: mining-induced and mining-triggered seismicity (McGarr and Simpson, 1997). The former is primarily driven by anthropogenic factors, with its frequency closely linked to the volume of extracted coal (Verdon et al., 2018). Most mining-induced seismic events are non-destructive, reflecting the natural stress response of coal and the surrounding rock mass (Whyatt et al., 2002). In contrast, mining-triggered seismicity involves interactions between mining operations and pre-existing geological structures. Mining

activities can act as catalysts in these cases, accelerating failures in geologically unfavourable zones and releasing significantly more energy than in typical induced seismicity (Stec, 2007).

Fault zones, common in coal mines, are especially prone to localised deformation and failure during mining activities due to their distinct geometric and rheological properties compared to surrounding rock formations (e.g. Lizurek et al., 2015; Ben-Zion, 2008; Bai and Konietzky, 2022). These high-risk zones pose challenges in understanding their hazardous characteristics, as the propagation of dynamic stress waves from fault slip can destabilise surrounding mine areas, thereby increasing the potential for secondary hazards. While geological mapping offers some insights into fault characteristics, its utility is limited in regions with minimal exposure. Moreover, the high costs and the need for skilled professionals for real-time monitoring further exacerbate these challenges (Andersen, 2001).

Microseismic (MS) monitoring technology offers an effective alternative solution to address these challenges. Identifying the seismic source is a foundational step in MS analysis, involving the determination of the hypocenter location and origin time. With advancements in the understanding of seismic phenomena, MS analysis has evolved beyond merely inferring fault geometry based on spatiotemporal attributes to exploring the intricate processes of rupture (e.g. Maxwell et al., 2015; Bai et al., 2019; Song et al., 2023). Focal mechanisms and source parameter calculations have been reaffirmed as robust seismological methodologies for examining mine seismic source rupture processes (e.g. Ma et al., 2019; Song et al., 2022). Built upon moment tensor (MT) theory, these methodologies meticulously quantify and elucidate source behaviour by utilising waveform characteristics across both temporal and spectral domains. The full MT solution is crucial for accommodating both double-couple (DC) and non-double-couple (non-DC) models, capturing the complex motions in mining-triggered and mining-induced seismicity (Rigby, 2024). Induced seismicity often shows significant non-DC components, while triggered events are generally characterised by dominant DC components (Cesca et al., 2013). MT decomposition, which includes isotropic (ISO) and deviatoric (DEV) components, provides flexibility in representing geologically plausible sources (Dahm and Krüger, 2014). The standard decomposition of MT involves extracting DC and compensated linear vector dipole (CLVD) components from the DEV (Jost and Herrmann, 1989). However, this specific constraint may not be suitable for complex strong tremors, as the motion might deviate from the fault plane. Consequently, a reference decomposition form requires further validation to address the limitations of the subjective standard method.

In addition, the increasing frequency of high-energy mining-related seismic events ($>10^5$ J) further complicates effective monitoring. Current monitoring systems, whether in-mine or using local seismic arrays, often function independently, lacking the necessary coordination and integrated analytical capabilities. In-mine arrays, in particular, are increasingly affected by waveform saturation due to the limited dynamic range of geophones in detecting high-energy events (Rudziński et al., 2017; Caputa et al., 2021). Although local seismic networks have not yet encountered this issue, their ability to independently and accurately characterise complex seismic sources is hampered by the limitations of standard MT decomposition methods. Addressing these challenges requires combining data from both in-mine and local networks, together with applying cross-temporal and cross-frequency inversion techniques. This integrated approach enhances the analysis of seismic events, addresses signal saturation issues, and minimises the potential for subjective interpretations.

Our study explores the complex rupture process of a mining-triggered local magnitude (M_L) 2.6 seismic event, recorded by the Shandong digital seismic network, which occurred on 10 September 2022 in the Yangcheng coal mine, Shandong Province, China (Fig. 1). Data from a multi-local network incorporating both in-mine and local seismic instruments across a variety of scales are utilised. By integrating data from this multi-local network and employing both full-waveform MT (FMT) and hybrid MT (HMT) inversion methods, along with calculating the source parameters of the Yangcheng seismic sequence between 7 September and 20 December 2022, we aim to provide valuable mechanistic insights. These findings are essential references for seismic source analysis in specific mining areas and provide valuable information for seismic monitoring and mitigation efforts in similar environments.

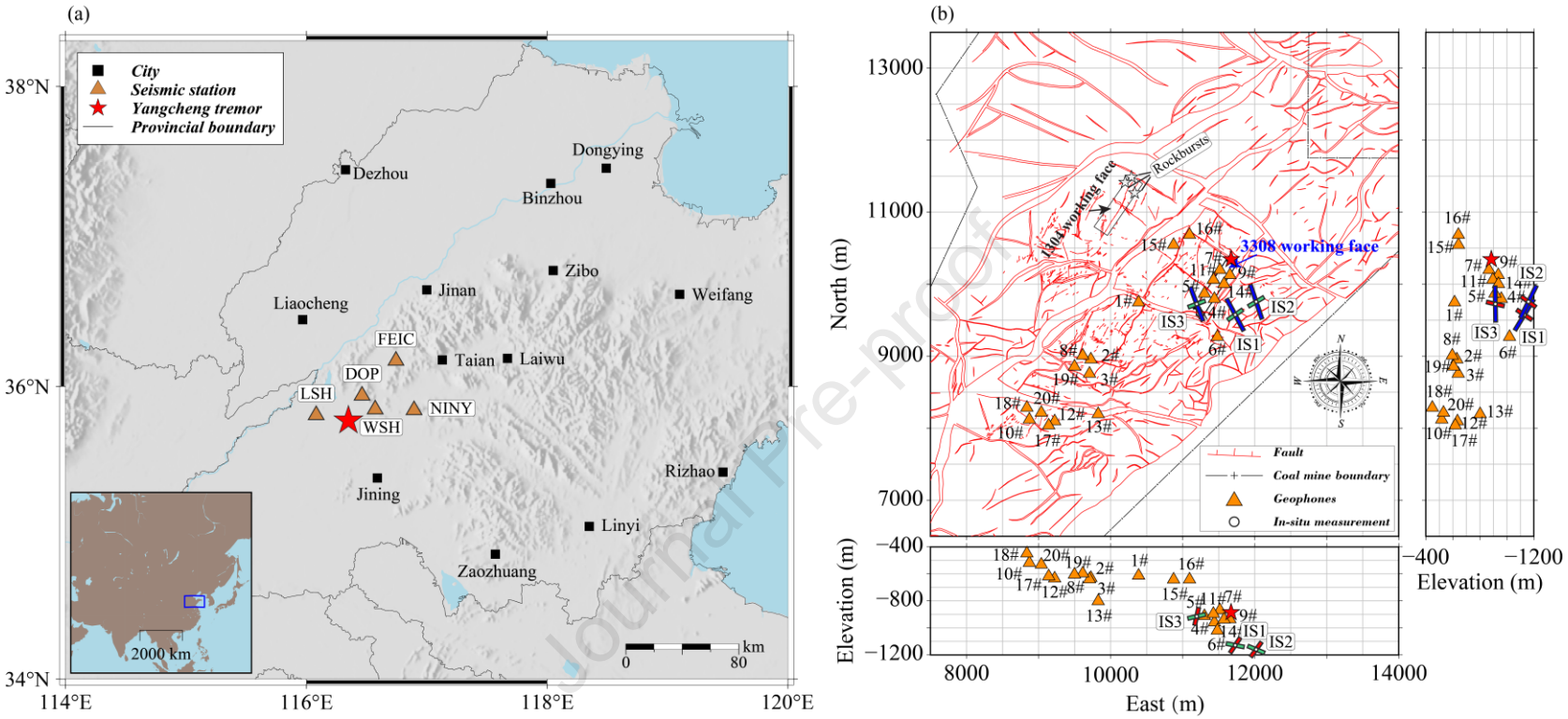

Fig. 1. Regional setting and location of the 10 September 2022 Yangcheng coal mine tremor (red star) relative to the multi-local network. (a) Three-component broadband local seismic stations (brown triangles with station codes). The study area is marked in the bottom-left corner inset. (b) Horizontal (N–E direction) and vertical cross-section (N–D and E–D directions) projection of short-period single-component geophones (orange triangles) of the in-mine network. The red lines represent surveyed faults within the mine and environs. The distribution characteristics of σ_H, σ_h, and σ_V, derived from in situ stress measurement (IS1–IS3), are denoted with blue, green, and red rectangles, respectively. Three white-filled stars indicate that the mine experienced three rockbursts.

2. Site and dataset overview

2.1. Engineering geology

The Yangcheng coal mine is in the Jibei Diggings of Jining City, Shandong Province, China, and is the largest underground coal mine in the province (Fig. 1a). The mining area covers 46 km^2, stretching approximately 10.5 km from north to south, with a width ranging from 2.2 km to 6.7 km from east to west. Geologically, the mine follows a primarily northwest-southeast (NW–SE) strike, inclined towards the northeast, with a dip ranging from 9° to 42°. The mine is characterised by a notable presence of faults (Fig. 1b), which have been located using three-dimensional (3-D) seismic data and confirmed by in situ mining activities. All faults, except for the FD66 fault, are categorised as normal. Also, faults are grouped into three categories based on their strike: NE–SW, NW–SE, and nearly EW.

Mining operations were initiated in 2007, targeting the #3 coal seam with a thickness ranging from 6.5 m to 8.3 m. However, due to the presence of faults, the mine experienced three significant rockbursts (Fig. 1b) during the initial mining phases from August to October 2012 at the 1304 working face (Jiang et al., 2016). Recently, an unusual tremor event occurred in the 3308 working face, drawing renewed attention from both operators and regulators. This event exhibited spatiotemporal similarity to the three rockbursts in 2012, as it occurred during the initial mining phases of the working face and in close proximity to faults. The 3308 working face (Fig. 2) is located in the southeast section of the mine on its eastern and western sides, which are bordered by the DF56 normal fault and 3306 goaf (February 2018–November 2019), respectively. Its southern and northern sides are adjacent to the -920 yard and DF60 normal fault, respectively. Detailed information about the internal and adjacent faults of the 3308 working face is provided in Table S1 (see supplementary material for details). The overall geological structure surrounding the working face is characterised by a NE–SW strike dipping to the SE. The mining area has a designated length of ~650 m and width of ~150 m. A fully-mechanised full seam top coal caving mining method was employed to extract the #3 coal seam with an average thickness of 7.5 m and a dip of 28°. The mining depth varies from 840 m to 960 m, with the mining level referenced to a datum (0 m) actually 39 m above sea level. Data from the in situ Y9-1 borehole (Fig. 2) indicate relatively homogeneous lithological attributes characterised by predominately fine-grained sandstones and siltstones. The immediate and primary roofs consist of siltstone and sandstone with thicknesses of 3.8 m and 17.1 m, respectively. The immediate and primary floors are composed of mudstone and fine sandstone with thicknesses of 1.6 m and 2 m, respectively.

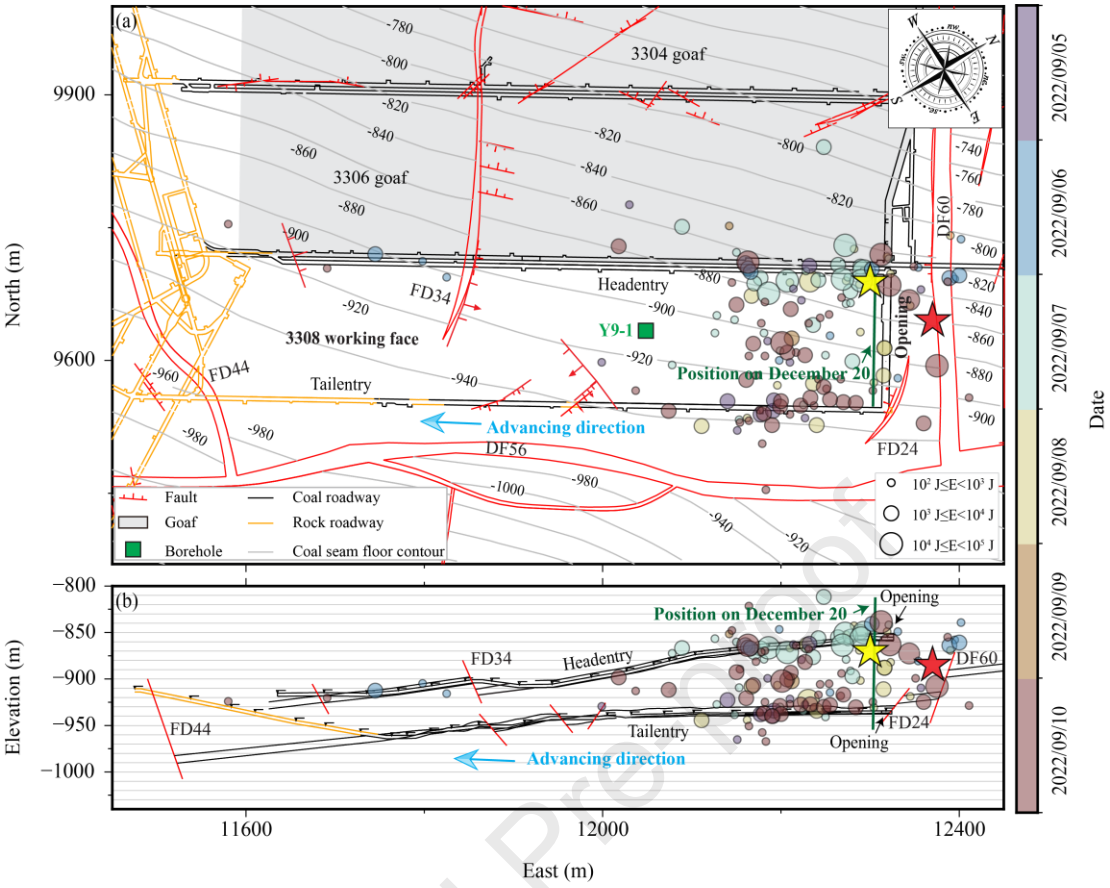

Fig. 2. Map (a) and cross-sectional view (b) of the MS event (circles) with locations obtained from the SOS between 5 September and 10 September 2022. Released energy and timing of the events are coded according to the legend and coloured bar. The red and yellow stars represent the 10 September 2022 tremor event and the 20 December 2022 aftershock, respectively. The grey-filled areas indicate the goaf, while the green square represents the Y9-1 borehole.

In situ stress measurements obtained from locations internal and adjacent (IS1–IS3) to the 3308 working face (Fig. 1b) reveal several parameters (Table S2). The maximum horizontal principal stress (σ_H) is oriented SSE–NNW (152°–161°) with a low plunge (-31°–1°) and magnitude in the range of 27 MPa to 32 MPa. The minimum horizontal principal stress (σ_h) is oriented ENE–WSW (55°–70°) again with a similar low plunge (-23°–13°) and magnitude in the range of 16 MPa to 21 MPa. The vertical stress (σ_V) is oriented ESE–WNW (114°–129°) with a high plunge (>50°) and magnitude of ~16 MPa. It is worth noting that the irregularly shaped opening in the 3306 goaf resulted from modifications made during reshaping after encountering roof collapse while expanding parallel to the DF60 fault (Jining Energy, 2017).

2.2. Multi-local network layout

In response to the occurrence of felt earthquakes, the Shandong Earthquake Administration of China took proactive measures by initiating the deployment of a localised surface seismic monitoring network in late 2006. This monitoring network covers an area of approximately 10 km × 50 km, effectively surrounding the entire Yangcheng coal mine. Equipped with five broadband three-component seismometers (including models FBS-3B and BBVS-60), the permanent seismic network (Fig. 1a) facilitates monitoring with a dynamic range exceeding 140 dB and a sampling rate of 50 samples per second.

In addition to the surface seismic monitoring network, an underground network is operational within the Yangcheng coal mine (Fig. 1b). This network is integrated into the Seismological Observations System (SOS) developed by the Department of Geology and Geophysics of Główny Instytut Górnictwa, Poland. It is designed for long-term, real-time monitoring of underground MS

activity. The underground network consists of 20 short-period single-component DLM-2001 geophones installed vertically on stable floors at depths ranging from 400 m to 1100 m (Fig. 1b). These geophones have a well-defined plateau in the amplitude-frequency response of 0.8–250 Hz and a sampling rate of 500 Hz. In addition, the signal transmission is in the form of a current, with a sensitivity of 15 A s/m. The geophones were calibrated in an absolute sense using the commercial software SEISGRAM, which is integrated into the SOS used for data acquisition. However, the limitations of the geophones, with a dynamic range ≤70 dB, resulted in clipped seismograms, particularly for the P- or S-waves. This issue became more pronounced during strong tremor events occurring in close proximity to the geophones, significantly affecting the resolved estimation of source strength. An evident illustration of this challenge is the saturation of signals observed by some geophones during an intense tremor event on 10 September 2022 (Fig. S1).

2.3. Catalogue characteristics and dataset screening

Mining operations at the 3308 working face began on 5 September 2022 but were suspended following a large tremor event on 10 September 2022 with an energy of 7.3×10^5 J. During this mining period, a total of 139 MS events with energies exceeding 10^2 J were recorded (Fig. 2 and Movie S1). Initial source locations were provided by the SOS and have been improved using Geiger's method (Geiger, 1912) with manually picked P-wave arrival times. The relocation hypocenter events shown in Fig. 2 are derived from a clockwise rotation of 58° around the local north-east-down (NED) coordinate system. The overall distribution of these events indicates a significant transition from the head entry to the tail entry and DF60 fault, with depth characteristics extending through the head entry floor and the tail entry roof. The monitoring catalogue recorded 76 events with energies between 10^2 J and 10^3 J, occurring consistently throughout the mining period and displaying a broad and seemingly random spatial distribution. Additionally, 52 events with energies ranging from 10^3 J to 10^4 J were primarily clustered (22 events) on the day preceding the tremor event. These events were predominantly located parallel to the tail entry and in proximity to the FD24 fault, with many occurring within the coal seam of the tail entry side. Notably, there were 11 events with energies ranging from 10^4 J to 10^5 J, with 5 instances each recorded on 7 September and 10 September 2022. Interestingly, the events during these two periods were separated by the opening of the 3308 working face. Specifically, those on 7 September 2022 were located on the southwest side of the opening, near the head entry, while those on 10 September 2022 were positioned on the northeast side, close to the DF60 fault. After discontinuing mining operations for 101 d after 20 December 2022, an attempt was made to resume mining at the working face, resulting in another high-energy event with (1.22×10^5 J). This event occurred at the intersection of the head entry and the opening, approximately 10 m below the coal seam floor.

To investigate the initial mechanism driving this strong tremor at the 3308 working face, we established a highly resolved dataset comprising 15 events, as shown in Table 1. These events were chosen based on strict criteria, including a high signal-to-noise ratio (SNR), clear and unambiguous P-wave first motions, and the necessary triggering of more than 10 geophones. This dataset serves as the foundation for the further investigation and analysis included here.

Table 1. Catalogue of the fifteen events selected from the 3308 working face.

Segments	No.	Date and time	East (m)	North (m)	Elevation (m)	f_c (Hz)	R (m)	$\Delta\sigma$ (MPa)	M_0 (N m)	M_w
Foreshocks	1	2022-09-07 05:06:43	11,566	10,262	-856	29.7	45.3	0.068	1.5×10^{10}	0.74
	2	2022-09-07 06:32:34	11,549	10,206	-866	20.2	66.5	0.069	4.7×10^{10}	1.08
	3	2022-09-07 06:33:18	11,549	10,308	-851	16.1	83.5	0.072	9.7×10^{10}	1.29
	4	2022-09-07 06:41:50	11,585	10,311	-850	21.2	63.4	0.14	8.1×10^{10}	1.24
	5	2022-09-07 11:48:34	11,549	10,232	-871	14.8	90.8	0.095	1.6×10^{11}	1.44
	6	2022-09-07 13:44:46	11,597	10,285	-854	34.3	39.2	0.055	7.5×10^{9}	0.55
	7	2022-09-07 15:53:54	11,606	10,230	-876	36.6	36.7	0.064	7.2×10^{9}	0.54
	8	2022-09-07 19:36:49	11,592	10,302	-856	32.5	41.4	0.081	1.3×10^{10}	0.71
	9	2022-09-08 15:55:14	11,580	10,285	-864	21.7	61.9	0.134	7.3×10^{10}	1.21
Mainshock	10	2022-09-10 14:38:25	11,673	10,346	-885	4.3	312.6	0.107	7.5×10^{12}	2.55
Aftershocks	11	2022-09-10 14:38:41	11,720	10,323	-908	20.9	64.3	0.133	8.1×10^{10}	1.24
	12	2022-09-10 14:38:55	11,640	10,333	-873	22.7	59.2	0.095	4.5×10^{10}	1.07
	13	2022-09-10 14:40:08	11,614	10,326	-863	17.4	77.2	0.092	9.7×10^{10}	1.29
	14	2022-09-10 15:51:19	11,589	10,338	-842	23	58.4	0.068	3.1×10^{10}	0.96
	15	2022-12-20 20:55:42	11,600	10,310	-872	14.6	90.1	0.284	5.1×10^{11}	1.77

Note: f_c, R, $\Delta\sigma$, M_0, and M_w represent corner frequency, source radius, static stress drop, scalar seismic moment, and moment magnitude, respectively.

3. Methodology

Failure within the physical source region can be regarded as a localised discontinuity within a continuum (Backus and Mulcahy, 1976). This can be described using a general second-order MT (3×3 matrix), which is compatible with the stress-strain tensor formulas commonly used in rock mechanics (Linzer, 2005). Importantly, this MT can represent diverse seismic source types, including expansion, double couples, and their combinations. The MT inversion process infers the physical response of the seismic source by optimising the inference of the inaccessible source from its observable external manifestations. Solving the inverse problem relies on Green's functions (GFs), which delineate the wave propagation between the hypocenter and receiver. The representation theorem for seismic sources (Aki and Richards, 2002) and the point source approximation describe the far-field displacement vector $\boldsymbol{u}$ at an arbitrary observation location $\boldsymbol{x}$ at time t, as given by Eq. (1):

$$u_n(\mathbf{x},t) = G_{ni,j}(\mathbf{x},\boldsymbol{\xi},t-\tau) * M_{ij}(\boldsymbol{\xi},\tau) \quad (1)$$

where $G_{ni,j}$ ($\boldsymbol{x}$, $\boldsymbol{\xi}$, $t - \tau$) is the ni-th component of the elastodynamic GF, which indicates the n-component of the displacement at observation spatial position $\boldsymbol{x}$ caused by the unit force component i applied at source coordinate $\boldsymbol{\xi}$ at time $t - \tau$. The comma in $G_{ni,j}$ denotes partial differentiation at the source with respect to coordinates ξ_j, i.e. $G_{ni,j} = \partial G_{ni}/\partial \xi_j$, and follows the Einstein summation convention. The M_{ij} terms are scalars representing the nine components of the MT, $\boldsymbol{M}$. The symbol '*' denotes the temporal convolution.

We utilise FMT inversion to analyse the seismic monitoring network data, outlining the cascading rupture sequence. In parallel, HMT inversion and source parameter calculations are employed for the Yangcheng seismic sequence. This dual approach focuses on identifying potential features, migration patterns, and mechanisms driving the mainshock. The most meaningful insights are extracted from the available data to address the core scientific questions driving this investigation by carefully selecting and

configuring the appropriate inversion techniques.

3.1. Full-waveform moment tensor inversion

The essence of the FMT inversion technique lies in its iterative optimisation process. We compare synthetic data derived from forward modelling using source models and GFs with observed data at each sampling point. The GF dataset comprises a 3-D grid of potential epicentral distances and hypocenters calculated through linear interpolation from a layered velocity model. This dataset was precomputed using the Fomosto software (Heimann et al., 2019), which integrates Qseis (Wang, 1999) and employs the Thomson-Haskell propagator method.

This iterative process determines the optimal MT by minimising the difference between observed and synthetic data, as specified in Eq. (2):

$$\Delta \boldsymbol{d} = \boldsymbol{d}_{\text{obs}} - \boldsymbol{d}_{\text{synth}} \tag{2}$$

where $\boldsymbol{d}_{\text{obs}}$ represents the observed data, refined outputs derived from the initial measurements. These refined outputs undergo various processing, including tapering to inversion seismic phases, restoring to displacement waveforms, and filtering. The terms $\boldsymbol{d}_{\text{synth}}$ refer to synthetic data, namely simulated seismograms, which are post-processed in a similar manner.

To minimise the heavy reliance on extensive iterations of the objective function, the Grond optimisation framework is employed (Heimann et al., 2018), which utilises the Bayesian bootstrap optimisation (BABO) algorithm. BABO is a specialised method that combines Bayesian inference with bootstrapping techniques to optimise the particular objective function, providing a probabilistic treatment of the inverse problem. This integration enables the quantification of parameter uncertainties and the generation of a range of plausible source models. Additionally, the parallelisation capabilities of the BABO algorithm within the Grond framework can significantly accelerate the optimisation process, making it a valuable tool for the analysis of earthquakes and other complex geophysical phenomena. Available as an open-source Python Pyrocko package (Heimann et al., 2017), the Grond framework with the BABO algorithm has proven effective in analysing earthquakes of various magnitudes at both local and regional scales (e.g. Dost et al., 2020; Kühn et al., 2020; Petersen et al., 2021). The BABO algorithm parameterises the MT parameters, including the moment magnitude (M_{w}) and six relative MT components (Eq. (3)), and involves stepwise optimisation to generate candidate source model spaces guided by standard deviation compensation:

$$\left.\begin{array}{lll} m_1 = M_{nn}, & m_2 = M_{ee}, & m_3 = M_{dd} \\ m_4 = \sqrt{2}M_{ne}, & m_5 = \sqrt{2}M_{nd}, & m_6 = \sqrt{2}M_{ed} \end{array}\right\} \tag{3}$$

where independent elements of the MT, denoted as m_1 to m_6, are defined in the NED coordinate system and derived from the Euclidean norm of the scalar seismic moment M_0. The numerical search range for m_1 to m_3 spans from $-\sqrt{2}$ to $\sqrt{2}$, and for m_4 to m_6, it extends from –1 to 1.

The details of the parameter configuration for the FMT inversion are included in the supplementary material Text S1.

3.2. Hybrid moment tensor inversion

Although FMT is typically robust, its application in mining environments faces certain limitations. Specifically, for low-energy events characterised by high corner frequency, FMT inversion is susceptible to waveform contamination from noise, resulting in artefacts characteristic of low SNR. Moreover, the high corner frequency corresponds to a short wavelength, subject to scattering and attenuation during propagation; thus, the receiver can only capture easily extractable P-wave arrival information. For high-energy events, achieving point-to-point assessment between saturated monitoring and synthetic traces becomes impractical.

These challenges are evident when utilising FMT inversions for the Yangcheng in-mine network data. However, the HMT technique tailored for mining, pioneered by Andersen (2001), has shown promise in overcoming the limitations of the FMT inversion. This technique integrates absolute and relative amplitude inversion methods, providing benefits beyond extracting only

the raw amplitude-phase data of interest. It also addresses sensor and path effects resulting from insufficient medium information by employing median and weighted mean corrections, given by Eq. (4) (Kwiatek et al., 2016). Therefore, we used the open-source HybridMT package (Kwiatek et al., 2016) to calculate the MTs of the underground dataset.

$$u_{ij}^{*,\mathrm{obs}} = u_{ij}^{\mathrm{obs}} + w_i u_{ij}^{\mathrm{obs}} \left(r_i - 1 \right) \tag{4}$$

where $u_{ij}^{*,\mathrm{obs}}$ and u_{ij}^{obs} represent updated and original displacement data, respectively. The w_i is a weighting factor ranging from 0 to 1. The optimal MT occurs when the iteration reaches a steady state for the ratio correction factor, i.e. $|r_i\text{-}1| < \varepsilon$. A detailed description and configuration parameters of the HMT technique can be found in Andersen (2001) and Text S2, respectively.

3.3. Source parameter calculation

The M_0 and M_w obtained from MT inversion allow for the estimation and comparison of earthquake intensities, following a logarithmic relationship, as shown in Eq. (5) (Hanks and Kanamori, 1979). Compared to M_L, M_w is more suitable for providing an effective static measure for high-energy mine tremors as it is theory-based as:

$$M_w = \frac{2}{3} \log_{10} M_0 - 10.7 \tag{5}$$

where M_0 (N m) represents the physical measure of strain energy released during an earthquake, while M_w converts this energy into a more intuitive seismic magnitude indicator. Regarding the calculation of M_0, in addition to the time-domain calculation mentioned earlier, Fourier transformation also permits its estimation in the frequency domain (Stork et al., 2014):

$$M_0 = \frac{4\pi\rho v^3 r \Omega_0}{F} \tag{6}$$

where ρ, v and r represent the density of the medium, P- or S-wave velocities, and 3-D (N, E, D) epicentral distance, respectively. F is a radiation pattern correction term, with values of 0.52 for the P-wave and 0.63 for the S-wave, respectively (Aki and Richards, 2002). Ω_0 is the low-frequency spectral amplitude value, which can be determined by fitting an ω^2 source model as in Fig. 3 (Brune, 1970):

$$\Omega(f) = \frac{\Omega_0 \mathrm{e}^{-\pi f t^*}}{\left[1 + \left(f / f_c \right)^2\right]} \tag{7}$$

where t, f, and f_c represent the travel-time, frequency, and corner frequency, respectively. t^* is the whole path attenuation operator for a ray propagating from the event to a receiver. Additionally, in the frequency domain, the calculation of the source strength also facilitates the acquisition of other source parameters besides f_c, such as the source radius R and static stress drop $\Delta\sigma$ (Brune, 1970):

$$\left.\begin{aligned} R &= \frac{kv}{f_c} \\ \Delta\sigma &= \frac{7M_0}{16R^3} \end{aligned}\right\} \tag{8}$$

where v is P- or S-wave velocity. k is the constant associated with the spherical average of corner frequencies, with values of 0.32 for the P-wave and 0.21 for the S-wave, respectively (Madariaga, 1976), and the detailed configuration parameters used can be found in Text S3.

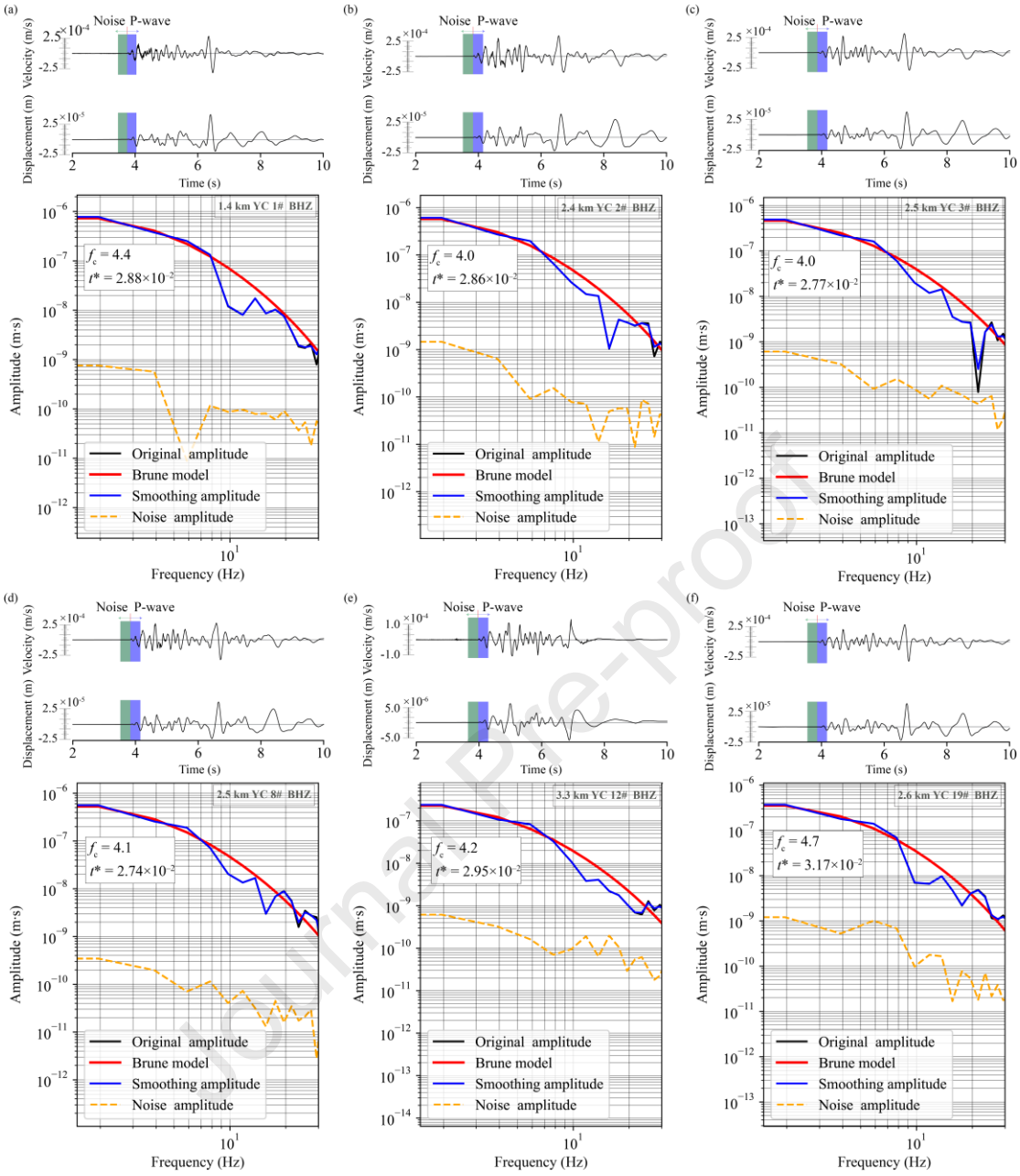

Fig. 3. Examples of spectral fitting for a displacement P-wave trace using a one-and-a-half cycle of log time window. Each panel, from top to bottom, depicts velocity seismograms from geophones, displacement seismograms obtained through integration, and the spectral fitting process for the geophones (vertical component BHZ), labelled (a) 1#, (b) 2#, (c) 3#, (d) 8#, (e) 12#, and (f) 19#. Green and blue shaded areas mark the noise and signal windows, respectively. The spectral fitting panel displays the original spectra (black line), smoothed spectra (blue line), noise spectra (orange line), and the best-fitting Brune spectra (red line). The legend in the top-right includes the 3-D epicentral distances, network, geophone code, and geophone component. The estimated f_c and t^* are shown in the top-left corner.

4. Results

4.1. Multi-local network moment tensor solution

The integration of FMT and HMT inversion techniques holds significant promise in addressing the inherent limitations of each method. By combining these complementary approaches, a comprehensive understanding of the mainshock source behaviour

within a multi-local network can be gained. The FMT inversion, for instance, helps compensate for information loss in the underground network, providing a more comprehensive view of the mainshock source mechanisms. In contrast, HMT inversion offers valuable insights into the spatio-temporal evolution of foreshocks and aftershocks. Thus, the FMT-HMT integrated approach presents a more robust and accurate characterisation of the seismic source behaviour, which is especially valuable in mining case studies.

The FMT inversion results shown in Fig. 4 exhibit a high degree of reliability, as evidenced by the good waveform fit in the time domain and the low global misfit of 0.32, resulting in an estimated M_w of 3.0. Analysis of the MT decomposition reveals a dominant non-DC component in the mainshock (Table 2). The percentages of the ISO, DC, and CLVD components are 54% (negative), 4%, and 42% (negative), respectively. The large, negative diagonal elements of the MT (M_{11}, M_{22}, M_{33}) are typical characteristics of collapse events reported in previous studies (e.g. Dreger et al., 2008; Ford et al., 2008; Pasyanos et al., 2023). Additionally, the focal mechanism indicates a normal faulting style, where the most probable fault plane trends ENE–WSW, deviating significantly by approximately 40° from the strike of the DF60 fault and dipping toward the SSE (Fig. 5).

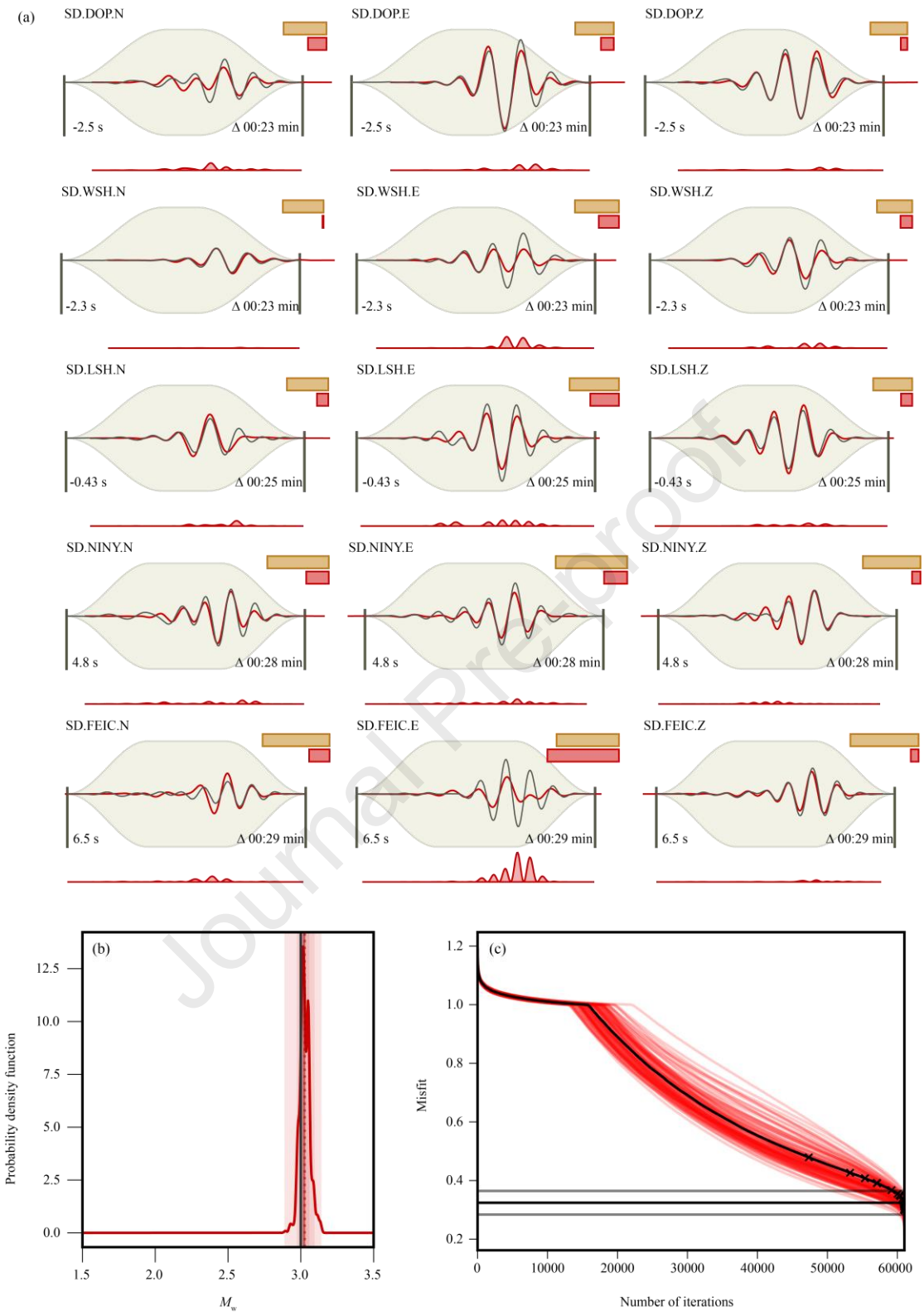

Fig. 4. (a) Fitting results of observed (black line) and synthetic (red line) traces filtered with a bandpass 0.1-0.3 Hz for the 10 September 2022 tremor event at five three-component stations in FMT. The network, station code, and station component are indicated in the top-left corner. Bars filled with brown and red in the top-right corner show the relative weights and residuals of each station, respectively. The beige-filled background represents the time window and taper function. The left-hand side value represents the onset time relative to the event origin, and the right-hand side value reflects the time interval between the two black marker lines. The bottom plane displays the amplitude residuals as a red distribution. Traces are normalized after being multiplied

by their respective weighting factors. (b) The recalculation of M_w is estimated through the probability density function within the model space ranging from 1.5 to 3.5. The overlapping red-shaded areas represent the 68% confidence intervals (innermost area), the 90% confidence intervals (middle area), and the minimum and maximum values (widest area). The solid and dashed red vertical lines represent the median and mean of the distribution, respectively. The optimal solution corresponds to the solid black vertical line. (c) Bootstrap misfit results. For each bootstrap configuration, all models are arranged according to their misfit value (red lines) and their global misfit value (black line), with each line being sorted individually. The best model from each bootstrap configuration (the model at the right end of the red lines) is marked as a cross in the global misfit plot. The horizontal black lines represent the mean, while the grey lines indicate the ± standard deviation of the y-axis values of these crosses.

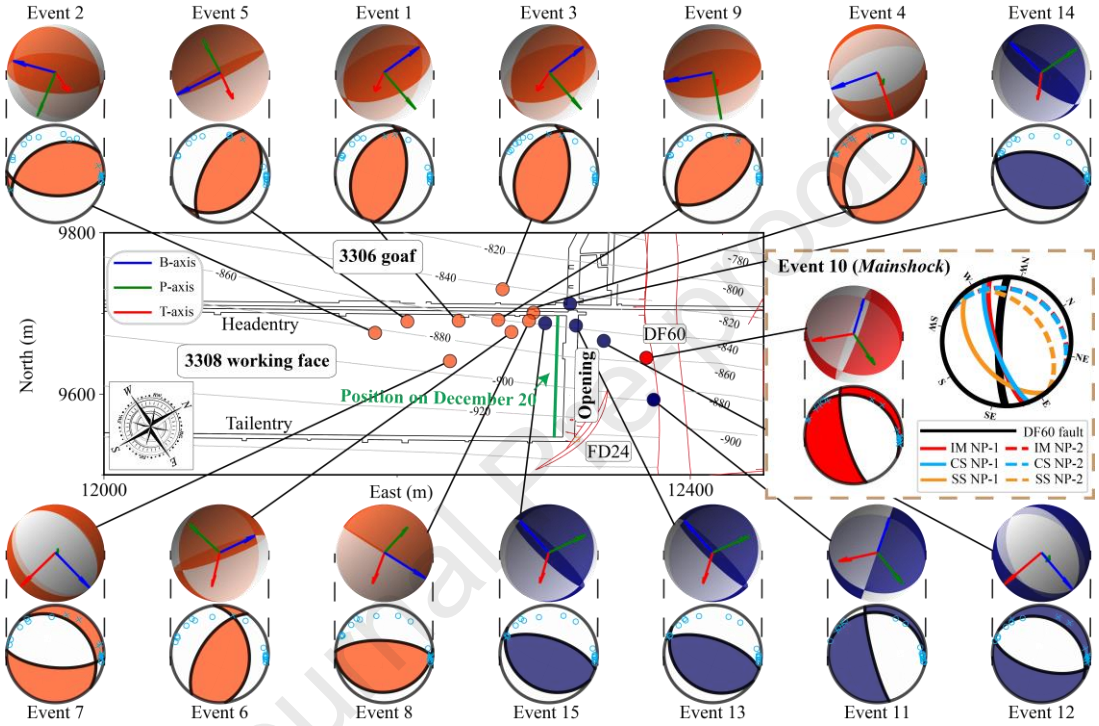

Fig. 5. Focal mechanism solutions of the Yangcheng seismic sequence based on the HYM method. The green, red, and blue lines in the 3-D beachballs show the pressure, tensile, and intermediate axes, respectively. Plane beachballs with geophone symbols are determined from the lower hemisphere stereographic projection, where 'x' and 'o' markers denote positive and negative P-wave polarities of the triggering geophones, respectively. Foreshocks, mainshock, and aftershocks are colour-coded by orange, red, and blue circles, respectively. The right side of the brown dashed rectangular box represents the geological projection of the DF60 fault (solid black line) and the focal mechanism solutions of the mainshock within the multi-local network. The solid and dashed lines represent nodal planes 1 and 2 for event 10 (mainshock), estimated using different approaches. The red lines, labelled 'IM NP-1' and 'IM NP-2', correspond to estimates made by the HMT within the in-mine network. The light blue lines, labelled 'CS NP-1' and 'CS NP-2', represent estimates derived from collapse model decomposition by FMT within the seismic network. The orange lines, labelled 'SS NP-1' and 'SS NP-2', indicate estimates obtained through standard MT decomposition by FMT within the seismic network.

Table 2. MT solutions for the 10 September 2022 tremor event obtained from the multi-local network.

Network	MT solutions						Nodal plane 1			Nodal plane 2			Standard decomposition			M_w	Misfit
	M_{11}	M_{22}	M_{33}	M_{12}	M_{13}	M_{23}	Strike (°)	Dip (°)	Rake (°)	Strike (°)	Dip (°)	Rake (°)	ISO	DC	CLVD		
In-mine	1.98×10^{12}	-5.99×10^{11}	-2.15×10^{12}	-3.90×10^{11}	-3.29×10^{12}	-1.31×10^{12}	106.9	76.1	-74.8	238.3	20.5	-36.8	-6	89	-5	2.38	0.11
Seismic	-1.29×10^{13}	-1.43×10^{13}	-4.36×10^{13}	-2.29×10^{11}	-1.77×10^{12}	-5.12×10^{11}	84.3	48.2	-88.1	261.4	41.9	-92.1	-54	4	-42	3	0.32

The robustness of the HMT inversion on underground data is primarily reflected in the high degree of polarity matching between theoretical and observed amplitudes, which generally exceeds 80% and reaches 100% for several key geophones (4#, 5#, 9#, 11#, 12#, and 17#) – a prerequisite in recovering stable focal mechanisms (Fig. S3). Regarding amplitude performance, corrections are required for geophones 4# and 17# by factors of approximately 2.2 and 2.6, respectively, while no adjustments are necessary for the other geophones. The corrected MT inversion results are presented in Table 3. To further illustrate the improvement offered by HMT inversion, we utilise the source-type plot, which projects the MT eigenvalues onto the fundamental lune of a unit sphere for visualisation (for specific details, see Tape and Tape, 2012a, b). As shown in the lune plot (Fig. 6), the MT solution refined by HMT inversion demonstrates a more pronounced clustering effect overall, indicating enhanced robustness and stability compared to the previous P-wave amplitude method.

Table 3. Focal mechanism solutions, standard decomposition of the full MT, M_w, and misfit derived from HMT inversion (mainshock in **bold**).

No.	Nodal plane 1			Nodal plane 2			Standard decomposition			M_w	Misfit
	Strike (°)	Dip (°)	Rake (°)	Strike (°)	Dip (°)	Rake (°)	ISO	DC	CLVD		
1	312.9	53.4	80.5	148.5	37.6	102.5	17	28	-55	0.55	0.34
2	34.8	53.1	108.3	185.9	40.6	67.3	2	71	27	1.09	0.13
3	309.8	56.9	78	151.1	34.9	107.7	-31	63	6	1.21	0.18
4	150.4	39.1	-105.9	350.6	52.7	-77.5	-23	65	-12	1.12	0.28
5	149.3	61.2	78.8	351.6	30.7	109.4	-13	44	-43	1.25	0.05
6	295.3	39.3	55.8	156.6	58.4	114.8	-11	11	-78	0.44	0.26
7	36.3	66.9	-108	255.9	29	-54.1	24	29	47	0.61	0.17
8	214.8	67.6	93.2	26.3	22.7	82.2	21	26	53	0.43	0.44
9	162.9	37.9	79.6	356	52.9	98	-6	49	-45	1.17	0.25
10	**106.9**	**76.1**	**-74.8**	**238.3**	**20.5**	**-36.8**	**-6**	**89**	**-5**	**2.38**	**0.11**
11	107.5	82.1	-75.6	225.7	16.4	-50.7	-11	63	-26	1.35	0.23
12	48.2	62.5	-96.2	241.5	28.1	-78.2	-51	3	-46	1	0.17
13	229.9	64.7	83.2	65.6	26.1	104.1	8	2	-90	1.37	0.14
14	225.1	55.6	84.2	55.2	34.8	98.3	-19	13	-68	0.83	0.33
15	229.5	63.4	83.3	64.3	27.3	103.2	-41	12	-47	1.72	0.14

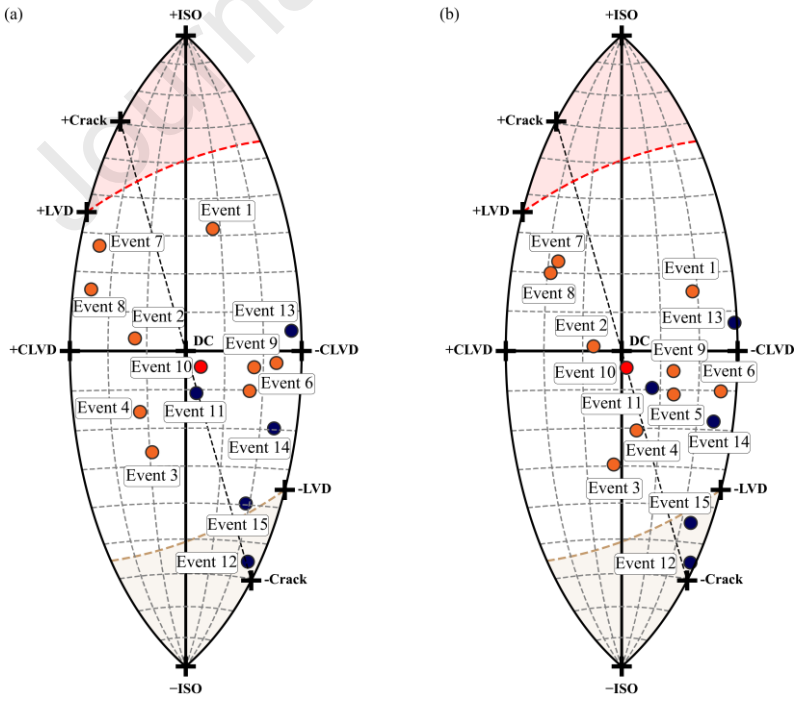

Fig. 6. Lune plots (Tape and Tape, 2012a, b) illustrate the source types of the Yangcheng seismic sequence determined by (a) the P-wave amplitude method and (b) the HYM method. The colours of the defined circles correspond to those used in Fig. 5.

The 15 events analysed in this study exhibit a diversity of failure modes, including tensile (events 1#, 7#, 8#, and 13#), compressive (events 6#, 12#, 14#, and 15#), shear (events 2#, 3#, 4#, 10#, and 11#) and composite failures (events 5# and 9#). This diversity covers all possible failure mechanisms related to coal-rock damage induced by mining activities, revealing the complexity of stress conditions in coal mining environments. The tensile failure may be attributed to elastic bending caused by the gravitational loading of overlying strata. Conversely, compressive failures are likely linked to stress concentration or localised compaction induced by mining activities (Wuestefeld et al., 2011). Shear failures, on the other hand, typically result from fault slip or dislocation within the coal or rock mass. The composite failures suggest the simultaneous influence of multiple stressors, potentially arising from the complex interaction of geological structures, mining activities, and coseismic deformation. Interestingly, the source types of events exhibited no apparent correlation with time, indicating that the failure mechanisms can vary significantly throughout different mining stages. This variability could be attributed to changes in geological conditions, mining activities, support conditions, and destress effects, reflecting complexity and randomness.

The focal mechanism solutions are represented in lower-hemisphere stereographic projections, with shaded and white regions indicating compression and dilation, respectively, considering the relative positions of geophones and P-wave polarities (Fig. 5). The event sequence shows two primary slip modes as five instances of normal faulting and ten instances of reverse faulting. The foreshock nodal plane strikes show variation, but the majority trend in just two directions: NNE–SSW (20°–40°) towards the DF60 fault and the SSE–NNW (140°–160°), aligning with the working face inclination (Fig. 7a). Foreshock plane dips also show significant variability, with most distributed between the ranges of 30°–40° and 50°–60° (Fig. 7b). In contrast, the aftershock nodal plane strikes display a more concentrated distribution, primarily striking ENE–WSW (40°–60°), approximately parallel to the 58° strike of the working face (Fig. 7c). The dips of the aftershocks show less variation, with the majority falling between 20°–30° and 60°–70°, correlating with the 26°–30° working face dip and foreshock-induced crack openings (Fig. 7d).

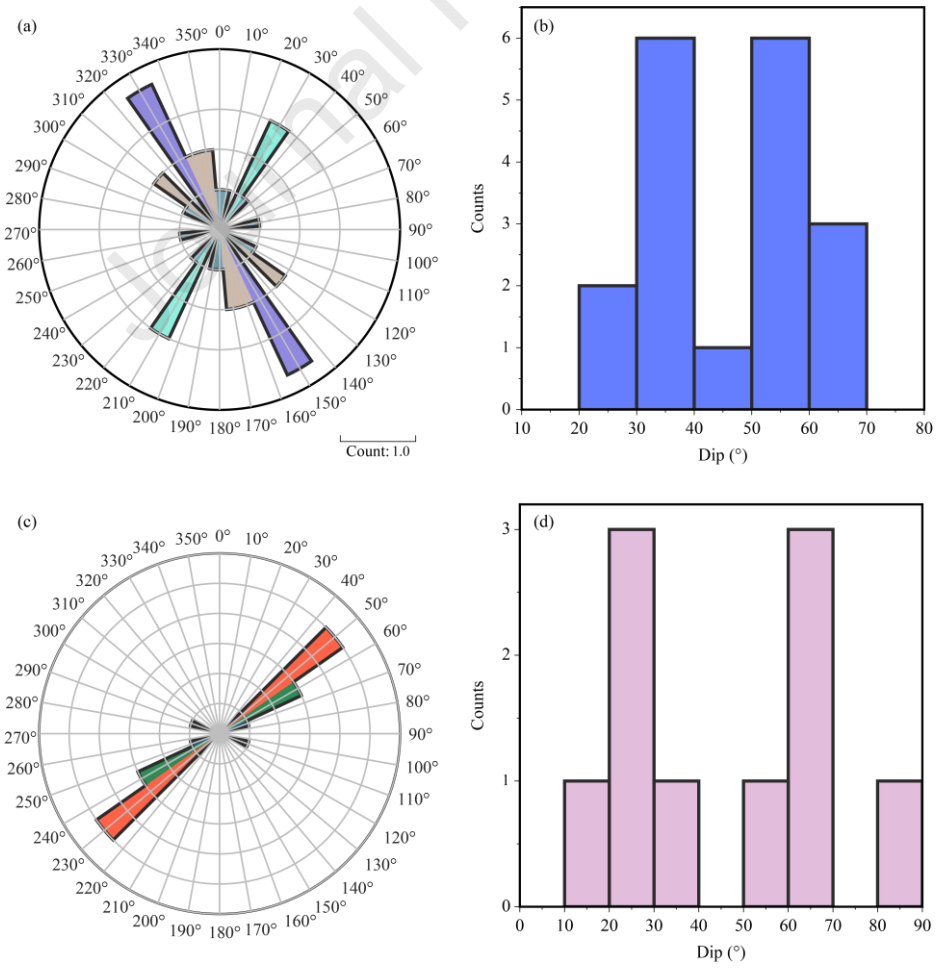

Fig. 7. Comparison of strike and dip of the fault plane for foreshocks and aftershocks. The first column contains rose diagrams ((a) and (c)) showing the strike distribution, while the second column has histograms ((b) and (d)) displaying the dip distribution for foreshocks (top panel) and aftershocks (bottom panel). The colours in the rose diagrams represent the count of events for each strike direction, and the histograms indicate the count of events for each dip angle.

The mainshock characteristics obtained from in-mine network inversion indicate that the tremor near the DF60 fault exhibits a shear failure typical of normal faulting. The most probable fault plane orientation is identified as having a strike of 106.9°, a dip of 76.1°, and a slip angle of -74.8°. This aligns closely with the characteristics of the DF60 normal fault, which has a strike of 123° and a dip of 80° (Fig. 5). Consequently, we infer that the mainshock is related to the activation of the DF60 fault. However, this finding contradicts the results of the seismic network inversion, which raises a fundamental issue regarding the mainshock mechanism. To address this apparent contradiction, we complete a closer examination of the source parameter calculations.

4.2. Source parameter analysis

The source parameters of 15 events estimated by spectral analysis are shown in Table 1. Magnitudes range from 0.54 to 2.55, aligning closely with those calculated in the time domain. The linear correlation between the two magnitudes (Fig. 8a) further validates the robustness of the inversion process. The relationship between f_c, ranging from 4.3 Hz to 36.6 Hz, and source strength metrics, M_0 and M_w, is illustrated in Fig. 8b. The overlain diagonals conform to the expected f_c-M_0 relationship described in Eq. (8), derived using assumed $\Delta\sigma$ values of 0.01 MPa, 0.1 MPa, and 1 MPa. Overall, the data exhibit the expected $M_0 \propto f_c^{-3}$ scaling, with M_0 tending to decrease as f_c increases along the diagonals. However, in rare individual events, a weak opposite trend is observed, potentially attributed to narrower f_c bands estimated by averaging across multiple geophones and a broader scaling of the parameter $M_0 f_c^3/v^3$ compared to the constant stress drop scaling (Naoi et al., 2022).

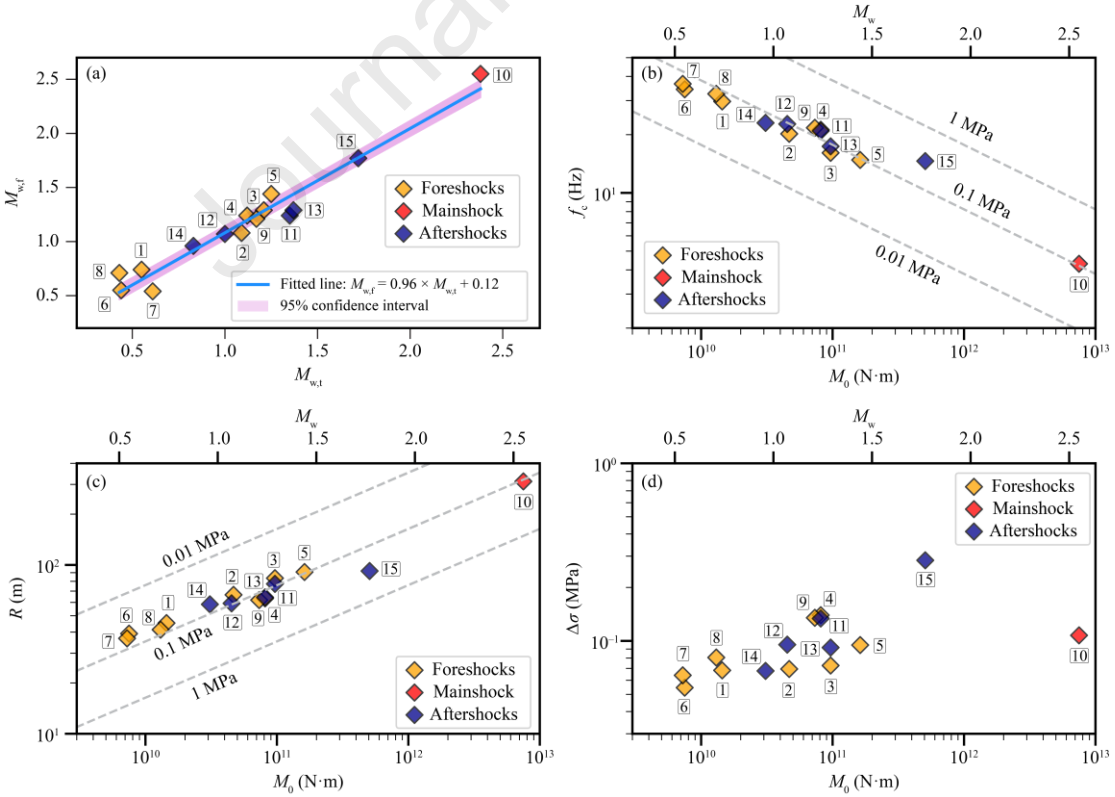

Fig. 8. (a) Comparison of M_w estimates obtained through the temporal domain ($M_{w,t}$) and spectral domain ($M_{w,f}$) calculations, depicted with a linear fit and 95% confidence intervals. (b) f_c-M_0-M_w relationship. (c) Relationship among R, M_0, and M_w. (d)

Relationship among $\Delta\sigma$, M_0, and M_w. The relationships shown in (b), (c), and (d) are the results of spectral-domain calculations. Diagonal lines indicating constant $\Delta\sigma$ are plotted as per the value of k = 0.32 and P-wave velocity (V_p) = 4200 m/s for Eq. (8). The colours of the Yangcheng seismic sequence with event codes correspond to those used in Fig. 5.

The rupture plane scaling R reflects the magnitude of coal and rock mass failure. Following the assumptions used for f_c (Eq. (8)), the diagonals show an upward trend as R increases, indicating a clear positive R-M_0 relationship (Fig. 8c). The estimated range of R in this study is 36.7 m to 312.6 m, with mainshock R values significantly greater than foreshocks and aftershocks. Stress drop $\Delta\sigma$, a crucial parameter for measuring stress changes around the failure source, has low estimated values from 0.05 MPa to 0.3 MPa. Unlike f_c and R, $\Delta\sigma$ shows no significant correlation with source strength (Fig. 8d) and demonstrates self-similarity within the M_w range. The notable variability among events of similar magnitudes is likely attributed to the increased sensitivity of the rupture zone to stress and strength heterogeneity (Calderoni et al., 2024). In complex underground environments, coal and rock mass failure are often influenced by high heterogeneity and multiple stress regimes, leading to adjustments in slip amounts based on the degree of heterogeneity (Ben-Zion, 2008). The resulting stress drop $\Delta\sigma$ is proportional to the ratio of slip amount to rupture size, with such variations more pronounced in cases of narrower rupture volume, dependent on local strength conditions (Calderoni et al., 2019).

5. Discussion

5.1. Complex rupture processes

The distinctiveness of the mainshock revealed by the source parameter calculation, along with the disparities in seismic MTs derived from the multi-local network, underscores the need for a more complex rupture model to elucidate this tremor event. In cases of strong (high-magnitude) mining seismicity, the rupture process is frequently characterised by intense 'shock-rebound' phenomena rather than simple shear sliding or tension-compression rupture. This dynamic process proves to be significantly more violent and heterogeneous than previously envisaged (e.g. Ohnaka, 1992; Gibowicz, 2009).

In the Book Cliffs Coal Mining District of Eastern Utah, Boler et al. (1997) reported a case of an M_L 3.6 seismic event where the confluence of diverse rupture processes was observed. Seismic analysis and on-site observations confirmed a larger-scale rupture following the initial seismic event, differing from the initially observed source mechanism. We infer that the seismic MT solution from the in-mine network reveals only the initial nucleation stage of the DF60 fault, with the released moment consistent with the M_w 2.55 DC model. The inversion results from the seismic network encompass the entire rupture process, where the normal faulting serves merely as a subset of the event. The high content of ISO (negative) and CLVD (negative) terms indicates the subsequent intense collapse process, reflecting strong nucleation morphology and moment release. Field investigations provide direct evidence for the subsequent rupture, showing floor uplift of the head entry side. Similar occurrences have been extensively documented in other coal mines. For example, Bai et al. (2021) demonstrated through numerical simulations that seismicity transitioned from the roof to the coal seam and floor during the fault activation stage, consistent with field observations. Moreover, Jiang et al. (2024) attributed this phenomenon to the secondary dynamic loading of the roof.

Studies by Talebi and Côté (2005) and Rudziński et al. (2016) suggest that under specific scenarios, a collapse event can be modelled using a tabular collapse model, represented by only three independent parameters, similar to a closing crack model in the z-plane. The corresponding moment density tensor is

$$\boldsymbol{M}^{\text{collapse}} = M_0^{\text{collapse}} \begin{bmatrix} -1 & 0 & 0 \\ 0 & -1 & 0 \\ 0 & 0 & \left(1-\frac{1}{\nu}\right) \end{bmatrix} \tag{9}$$

where $M_0^{\text{collapse}} = \lambda S D_N$, D_N is the average closure displacement on the crack with area S. $\nu = \lambda/2(\lambda+\mu)$ where ν represents Poisson's

ratio, and λ and μ are Lamé constants.

In this context, we apply the MT decomposition method proposed by Ford et al. (2008) to decompose the full MT $\boldsymbol{M}^{\text{full}}$ into $\boldsymbol{M}^{\text{collapse}}$ and residual MT $\boldsymbol{M}^{\text{rem}}$, stripping away the seismic rupture process. Here, $\boldsymbol{M}^{\text{rem}}$ represents physical processes other than geological collapse. However, harsh field conditions limit the use of geological fracture mapping techniques to estimate the contribution of $\boldsymbol{M}^{\text{collapse}}$, posing challenges for subsequent evaluation. Fortunately, an alternative scheme based on minimum residual was proposed by Rudziński et al. (2016), given by Eq. (10).

$$\boldsymbol{M}^{\text{full}} = \boldsymbol{M}^{\text{dc}} + \boldsymbol{M}^{\text{collapse}} + \boldsymbol{\varepsilon} \tag{10}$$

where $\boldsymbol{M}^{\text{dc}}$ represents the DC component, with normalised elements configured through an iterative grid search for possible orientations. The $\boldsymbol{M}^{\text{collapse}}$ diagonal moment ratio, expressed as [–1: –1: –3], is estimated based on Poisson's ratio (v = 0.25) from the 1-D velocity model in the Jining area. The scalar moments of $\boldsymbol{M}^{\text{dc}}$ and $\boldsymbol{M}^{\text{collapse}}$ are derived using the generalised inverse matrix. The minimum residual ε corresponds to the optimal MT decomposition scheme and the focal mechanism solution.

The resolved DC component has a scalar seismic moment of 2.2×10^{12} N m, M_w 2.2, with the most probable orientation having a strike of 102°, dip of 74°, and rake of -76°. To assess differences among fault planes before and after recalculation and those within the in-mine network, the smallest space rotation angle (Kagan, 1991), known as the Kagan angle, was used for precise quantification. The results show that the alternative decomposition scheme reduces the Kagan angle from 34° to 5° compared to the standard decomposition, indicating a remarkable agreement of geological parameters with the DF60 fault (Fig. 5). Furthermore, the resolved M_w 2.2 exhibits minimal deviation in source strength compared to the M_w 2.4 of the DC term derived from the in-mine network, a discrepancy attributed to the scattering and attenuation of seismic waves.

The resolved scalar seismic moment of the collapse component is 3.3×10^{13} N m, corresponding to a M_w 3.0 event. Due to the significant contrast in contribution with the DC component, we can reproduce the strongest nucleation displacement through forward modelling. The source model used for calculations is based on the $\boldsymbol{M}^{\text{collapse}}$. Fig. 9 shows the fitting results between the observed and synthetic seismograms at five stations. The collapse model effectively matches the strongest moment release under high-amplitude conditions. In conclusion, this high-magnitude tremor event likely stems from mining-triggered normal faulting nucleation followed by intense collapse.

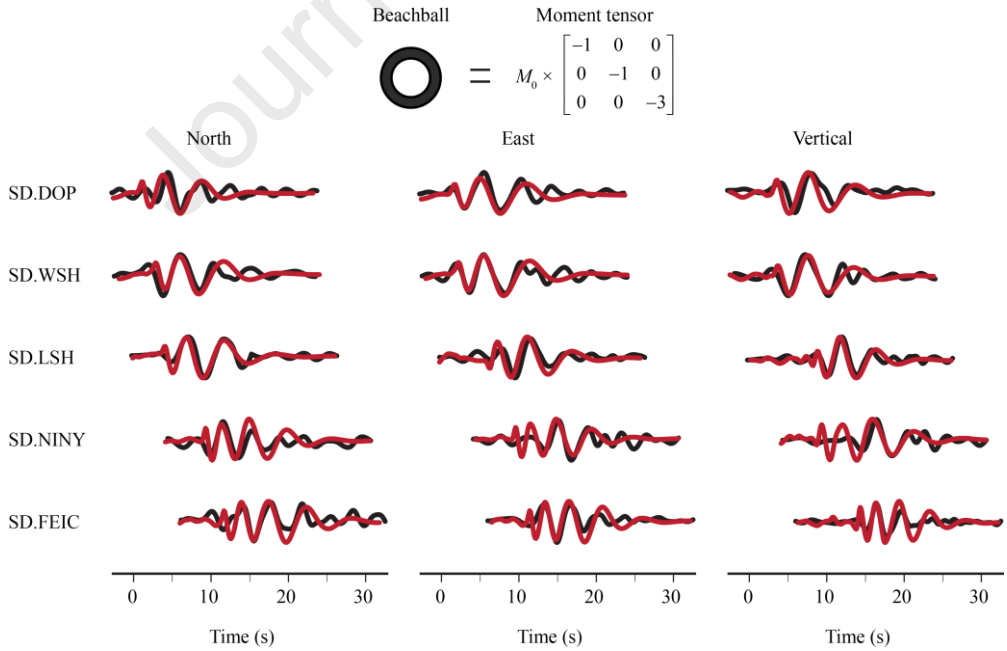

Fig. 9. Comparison of recorded (black line) and synthetic (red line) seismograms obtained through forward modelling of a pure vertical collapse mechanism (top plane). The seismograms are shown for 5 three-component (North, East, Vertical) seismic stations: SD.DOP, SD.WSH, SD.LSH, SD.NINY, and SD.FEIC. The moment tensor derived from this collapse model is represented by a black beachball, with a M_0 of 3.3×10^{13} N m.

The successful application of the tabular collapse model to separate complex cascading rupture sources has led to a reassessment of the limitations inherent in the generalised standard decomposition of the MT. Closely spaced seismic events from cascading ruptures within fault networks are difficult to distinguish using the standard method. The standard decomposition forces the CLVD and DC components to share the pressure or tension axis (tension axis for a positive CLVD), causing interference between the physically distinct rupture processes and leading to significant distortions. This forced approach erroneously merges the cascading ruptures into a single process, misrepresenting the true seismic source. The issue was addressed by demonstrating six different component combinations, with the cascading rupture represented by a normal fault mechanism source from this study and a negative vertical CLVD source (Fig. 10). The scalar moment of a cumulative source remains constant and is represented by the zero-trace DEV component. It is evident that the relative contributions of different physical source components in complex ruptures are highly sensitive to the standard MT decomposition. Specifically, an increase in a negative vertical CLVD component can introduce a Kagan angle of up to 34.1°. This high proportion of negative vertical CLVD is indeed encountered in this study. When the DC component dominates the cascading rupture source, the main issue becomes the CLVD being incorrectly oriented by the DC, particularly pronounced in the case of a reverse fault and a negative vertical CLVD (Fig. S4). These limitations are not restricted to coal mining environments but also extend to seismic events with complex source mechanisms in the contexts of volcanic (Gudmundsson et al., 2016) and nuclear explosions (Cesca et al., 2017).

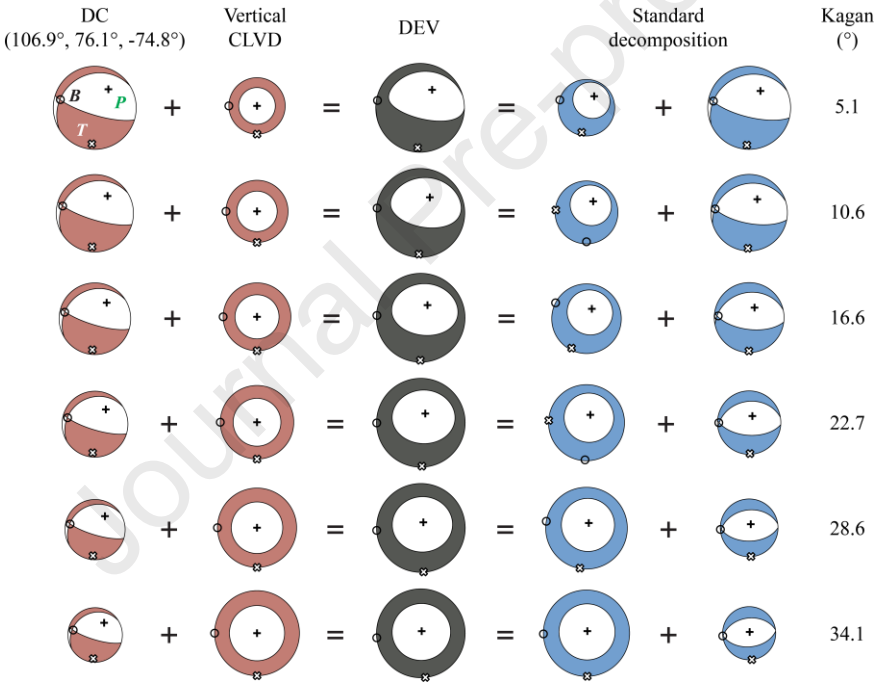

Fig. 10. Illustration of MT decomposition ambiguity. The left column depicts a combination of a normal faulting mechanism from this study and a negative vertical CLVD component in varying proportions. The relative size of the beachball corresponds to the proportion of each component, arranged from top to bottom as 17:3, 7:3, 11:9, 2:3, 1:3, and 1:9. The middle column shows the DEV component derived from the simulated MT. The right column displays the DC and CLVD components obtained from the standard decomposition of the DEV component in the middle column (Jost and Herrmann, 1989). The Kagan angle (Kagan, 1991) quantifies the deviation between the decomposed and actual DC components.

5.2. Mechanism of strong tremor

After gaining insights into the complex rupture process of the strong tremor event, it is essential to investigate the factors that triggered this seismicity. Examining the stress evolution characteristics and the radiation pattern of source clusters provides key insights into the most probable initiating scenario.

Before mining initiated at the 3308 working face, the sectional coal pillar in the head entry area and the irregular coal pillar near the opening of the 3306 goaf experienced stress transfer from the overlying strata of the 3306 goaf due to the stress arching effect (Zhao et al., 2018). This resulted in high stress concentration, especially at the corners of these coal pillars. As mining operations commenced, the goaf area expanded, advancing and lateral abutment pressures persistently acted on the 4 m wide sectional coal pillar on the northwest side of the head entry. This stress redistribution process is supported by the occurrence of nine foreshocks along the head entry, indicating ongoing fracturing and weakening of the sectional coal pillars, with abutment pressure increasingly affecting the DF60 fault and the tail entry along the floor (Kang et al., 2022). The direction of stress propagation is confirmed by the fault plane orientation of foreshocks and the spatiotemporal distribution characteristics of subsequent MS events (Movie S1).

The DF60 fault, which spans the entire No. 3 mining area and has a history of rockburst incidents, was eventually activated by continuous mining activities. Persistent stress led to the activation of normal faulting along the DF60 fault. Regarding the significant subsequent collapse, our hypothesis suggests that as the mining area of the 3308 working face expanded, horizontal constraints on the FD24 and DF60 faults decreased, leading to an increase in maximum horizontal principal stress along the strike of the working face. When this stress exceeded strength, shear stress on the fault plane caused the faults to unlock and slide relative to each other. Rapid subsidence of the overlying strata then occurred due to self-weight, resulting in severe collapse (Fig. 11).

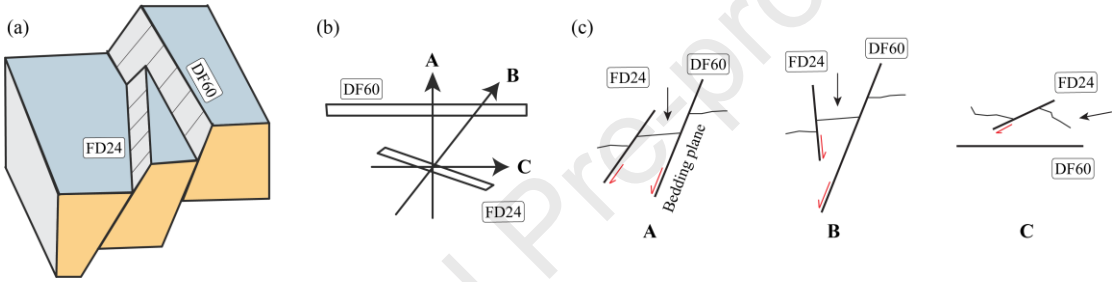

Fig. 11. Cartoon showing movement pattern of FD24 and DF60 faults and collapse model in (a) 3-D view, (b) plane view, and (c) profile view along directions A, B, and C in (b). FD24 and DF60 undergo normal faulting and continue to collapse under the influence of gravity.

It is noteworthy that the distribution of aftershocks indicates ongoing separation, detachment, and displacement of strata. Unlike the mainshock, these aftershocks primarily arise from the activation of pre-existing fracture networks, particularly at the intersection of the head entry and opening. Moreover, with the temporary suspension of mining operations, the rate of stress-driven processes has diminished, leading to a more gradual progression of collapse but with no significant moment release. Notably, event 15# in the aftershock sequence occurred after a stable period of 101 d. Influenced by mining-induced stress, it exhibited a significant ISO component with substantial negative values. Following the event, an immediate roof collapse was observed beneath the opening intersecting with the FD24 fault instead of the expected stope closure. As highlighted by McGarr (1992) and Yamada et al. (2007), this can be attributed to the re-closure of pre-existing fractures, emphasising the ongoing risk of secondary activation of the FD24 and DF60 faults.

5.3. Insights from seismic sequence source parameters

In natural earthquakes, foreshocks usually precede the main fault plane rupture, releasing stress earlier and involving more significant stress adjustment, while aftershocks follow the mainshock or occur near secondary ruptures adjacent to the primary fault plane. Conventionally, it is assumed that foreshocks exhibit higher stress drop $\Delta\sigma$ compared to aftershocks. However, this expected pattern diverges from observations in the coal mine environment investigated in this study. The deviation can be attributed to the unique characteristics of mining-induced seismicity, where the occurrence of foreshocks and aftershocks is influenced more by factors like mining layout, intensity, and the degree of local stress concentration rather than being strictly confined within geological structures. This scale-independent self-similarity does not conform to the conventional classification of foreshocks and

aftershock clusters. Fig. 12 compares the source parameters of our study with those occurring earlier within the Laohutai coal mine (Chen et al., 2021) and natural earthquakes (Abercrombie, 1995). Apart from the mainshock, our research observations are highly consistent with the stress drop $\Delta\sigma$ levels in coal mines, maintaining significant differences from natural earthquakes. This suggests that mining-induced seismicity exhibits characteristics of heterogeneity in stress and strength within confined spatial domains. However, the mainshock, with its distinct characteristics compared to other mining-induced events and natural earthquakes, is likely the result of mining-triggered.

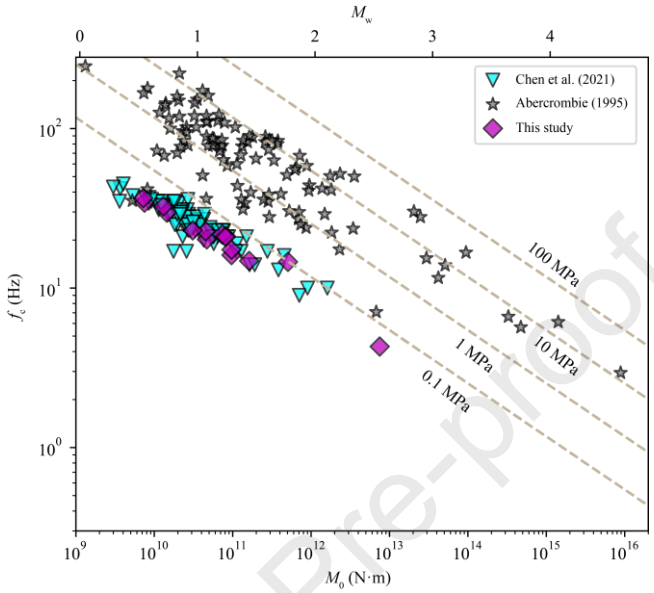

Fig. 12. Comparison of the measured f_c with results from other studies reveals a consistent trend of decreasing f_c with increasing M_0. The trend lines are constant $\Delta\sigma$ using an Abercrombie (1995) source model for comparison. The majority of the studies demonstrate a similar pattern of decreasing f_c as the M_0 increases, modified as per what is used to draw constant $\Delta\sigma$. Colours and geometric shapes are used to distinguish our study (purple diamonds), mining-induced seismicity (cyan triangles) modified after Chen et al. (2021), and natural earthquakes (grey stars) modified after Abercrombie (1995).

Upon a thorough examination of the seismic source parameters within the dataset, it becomes evident that the fluctuations in seismic source parameters for foreshocks directly related to mining are notably greater than those for aftershock sequences, with the exception of event 15# (Fig. 8). Event 15# merits separate discussion due to its repetitive reactivation by mining activities. For clarity, unless otherwise specified, aftershocks hereafter refer to those events excluding event 15#. The outlier characteristics of foreshocks may suggest different roles played by foreshocks and aftershocks in stress and structural adjustments within the underground strata. Specifically, the heightened volatility observed in foreshock source parameters likely reflects the immediate response of the coal and rock mass to mining. As mining progresses, cracks rapidly extend, leading to an upward trend in the R and M_w of foreshocks 1#–5#. Subsequent to significant fractures within the coal and rock mass, stress accumulation recommences, culminating in the reappearance of foreshocks 6#–9#, displaying similar trends of escalating R and M_w as observed in foreshocks 1#–5#. However, the source strength during this phase appears to have notably diminished compared to the previous phase. This phenomenon could be attributed to initial crack extension hindering stress transfer, thereby preventing the re-concentration of accumulated stress in specific areas, as observed during the initial accumulation phase.

Aftershocks exhibited stable fluctuations in source strength distinct from foreshocks, likely influenced by stress release and rock layer adjustments following the mainshock rupture. As noted by Brune et al. (1986), stress release on a fault plane is not uniformly distributed, potentially leading to partial stress events rather than simultaneous rupture across the entire fault, resembling a series of multiple events. In our case, the aftershock sequence is situated on the hanging wall of the DF60 fault and exhibits significant variation in the stress drop $\Delta\sigma$, further supporting our hypothesis.

Event 15# stands out in both its MT components and source parameters. After a prolonged period of stress adjustment, the event location returned to the source concentration area at the intersection of the head entry and opening (Fig. 5). The spatiotemporal behaviour of this event suggests a delayed reactivation, possibly linked to creep in the coal and rock mass in this area (De Santis et al., 2019). Additionally, the high source strength characteristics of this event are attributed to the coal rock structure near the intersection, facilitating both static and dynamic stress transfer (Masethe et al., 2023) and resulting in the closure of the pre-existing fracture network.

5.4. Future Perspectives and Implications

Underground mining and excavation activities alter stress regimes and release displacement constraints, significantly influencing subsequent mining-related seismicity characteristics (Linzer et al., 2021). Studies have shown that triggered seismic events exhibit similar phenomena to fault reactivation mechanisms in tectonic earthquakes (e.g. Donnelly and Rees, 2001; Stec, 2007; Yabe et al., 2015; Wang et al., 2019). For example, in a deep South African gold mine, Ortlepp (2000) observed that fault reactivation led to energy transmission into the surrounding rock rather than causing substantial shear damage to the intact rock mass. Similarly, Heesakkers et al. (2011) documented an M 2.2 event in the Archaean Pretorius fault structure in the TauTona mine, South Africa. This event, again triggered by fault reactivation, resulted in fresh fractures branching from the slip segment and extending in shear-tensile modes.

At the Lucky Friday Mine in northern Idaho, USA, Sprenke et al. (2002) conducted a fault plane solution analysis of seismic events using five high dynamic-range temporary stations. The results showed significant discrepancies between the calculated outcomes and actual damage in the mine. They speculated that this could be related to gradual slip, ultimately leading to sudden implosion damage of the stope margins. However, interpreting seismic events through various analytical methods remains a topic of debate. A notable example of the challenges in seismic risk management occurred at the Xinjulong coal mine in Shandong Province, China. A rockburst with an M_L 2.49 on 22 February 2020 resulted in 14 people being trapped and 4 fatalities. This event highlighted the critical importance of improved safety protocols. Occurring within a fault network comprising the FD6 and FD8 faults, Cao et al. (2021) used mechanical analysis and numerical calculations to link the event to a graben structure formed by these faults. The overloading of this structure, due to the large-scale hanging of the working face and overlying strata, triggered the seismic event. Alternatively, Song et al. (2024) utilised saturated underground network data for MT inversion and proposed that a shear slip of the FD8 fault caused the event.

These examples highlight the challenges in understanding the mechanisms behind mining-related seismicity. While current research has addressed the source mechanisms of complex cascading ruptures, inherent limitations need to be acknowledged to guide future work. The limited dynamic range of geophones restricts the capture of waveform data, particularly S-waves, which is vital for resolving dynamic source parameters and the relationship between rupture types and these parameters. Event magnitudes and unfavourable environmental SNR also constrain the effectiveness of multiscale networks in expanding the event catalogue for detailed rupture characteristics and long-term seismic evolution monitoring. The specific applicability thresholds of such networks across mining-induced seismicity magnitudes remain poorly defined.

To comprehensively address these complexities and limitations, future research should focus on several key areas. Enhancing data acquisition techniques, integrating emerging technologies such as machine learning and artificial intelligence, and implementing long-term monitoring strategies of multiscale networks are all crucial. Furthermore, validating inversion models in diverse geological conditions and integrating seismic data into real-time risk management systems are essential in bridging existing gaps. Addressing these areas will not only advance the field of mining-related seismicity research but also contribute to safer and more efficient mining practices overall.

6. Conclusions

This study employs MT inversion and source parameter extraction from a multi-local network to understand the rupture

mechanism in mining-related seismicity in a fault network at the 3308 working face of the Yangcheng coal mine in Shandong Province. The key conclusions drawn from this study are summarised as follows:

(1) The MT inversion of the multi-local network reveals the intricate rupture process involved in mining-triggered seismicity and accommodating large events. It reveals that the rupture initiates with normal faulting along the known DF60 fault, trending ESE–WNW, followed by a significant collapse possibly associated with relative slip resulting from the unlocking of FD24 and DF60 faults.

(2) Collapse events then result from complex interactions among multiple factors, making standard MT decomposition inadequate for comprehensively addressing the intricate rupture processes in coal mines, particularly because of the constrained geometric parameters of the DC and CLVD components.

(3) Following a 101-day period of stress adjustment, event 15# within the seismic cluster area positioned at the intersection of the head entry and opening, experienced reactivation. This delay is attributed to coal and rock mass creep, with seismic strain release from stress transfer to the pre-existing fracture network, indicating a heightened risk of secondary fault activation on the FD24 and DF60 faults.

(4) From source parameter analysis, it is clear that mining-related seismicity differs from natural earthquakes. Mining-induced events often exhibit scale-independent self-similarity and stress heterogeneity unaffected by geological structures. Foreshock parameters vary significantly, indicating an immediate response of the coal and rock mass strata to mining. Aftershocks display consistent strength fluctuations, possibly due to stress release and stratum adjustments post-mainshock rupture.

(5) Even small stress drop $\Delta\sigma$ near tectonically stressed areas can result in significant hazards in the underground, highlighting the importance of utilising MT inversion and source parameters estimation from multi-local networks to mitigate hazards. While working on the 3308 working face has been discontinued for two years, other mining operations continue in areas where hazards were previously unidentified, emphasising the significance of joint analysis of multi-local network data in revealing latent hazards.

Declaration of competing interest

The authors declare that they have no known competing financial interests or personal relationships that could have appeared to influence the work reported in this paper.

Acknowledgments

The Reviews provided by the editor and two anonymous referees significantly improved this manuscript. The authors would like to express their gratitude to Łukasz Wojtecki for his detailed explanation and guidance regarding the instrument information within the SOS system. Derek Elsworth gratefully acknowledges support from the G. Albert Shoemaker endowment. This study was funded by the National Natural Science Foundation of China (Grant No. 51574225), Shandong Energy Group (Grant No. SNKJ2022BJ03-R28) for Caiping Lu, and the Research Team on Monitoring and Activity Mechanisms of Unnatural Earthquakes of Shandong Earthquake Agency (Grant No. TD202301) for Chengyu Liu.

Appendix A. Supplementary data

Supplementary data to this article can be found online at XXX.

References

Abercrombie, R.E., 1995. Earthquake source scaling relationships from −1 to 5 ML using seismograms recorded at 2.5-km depth. J. Geophys. Res.: Solid Earth 100 (B12), 24015–24036.

Aki, K., Richards, P.G., 2002. Quantitative seismology, 2nd ed. University Science Book, Sausalito, California.

Andersen, L.M., 2001. A Relative Moment Tensor Inversion Technique Applied to Seismicity Induced by Mining, PhD Thesis.

University of the Witwatersrand, Johannesburg.

Backus, G., Mulcahy, M., 1976. Moment tensors and other phenomenological descriptions of seismic sources—I. Continuous displacements. Geophys. J. Int. 46 (2), 341–361.

Bai, Q., Konietzky, H., 2022. Numerical Insight Into Energy Partitioning During Stick-Slip Events Based on the Framework of Rate-and-State Friction Law. Geophys. Res. Lett. 49 (9), 2021GL096677.

Bai, Q., Konietzky, H., Ding, Z., Cai, W., Zhang, C., 2021. A displacement-dependent moment tensor method for simulating fault-slip induced seismicity. Geomech. Geophys. Geo-Energy Geo-Resour. 7, 1–25.

Bai, Q., Tibbo, M., Nasseri, M.H.B., Young, R.P., 2019. True triaxial experimental investigation of rock response around the mine-by tunnel under an in situ 3D stress path. Rock Mech. Rock Eng. 52, 3971–3986.

Ben-Zion, Y., 2008. Collective behavior of earthquakes and faults: Continuum-discrete transitions, progressive evolutionary changes, and different dynamic regimes. Rev. Geophys. 46 (4), RG4006.

Boler, F.M., Billington, S., Zipf, R.K., 1997. Seismological and energy balance constraints on the mechanism of a catastrophic bump in the Book Cliffs Coal Mining District, Utah, USA. Int. J. Rock Mech. Min. Sci. 34 (1), 27–43.

Brune, J.N., 1970. Tectonic stress and the spectra of seismic shear waves from earthquakes. J. Geophys. Res. 75 (26), 4997–5009.

Brune, J.N., Fletcher, J., Vernon, F., Haar, L., Hanks, T., Berger, J., 1986. Low stress-drop earthquakes in the light of new data from the ANZA, California telemetered digital array. Earthquake Source Mechanics, Geophysical Monograph 37, 237–245.

Calderoni, G., Improta, L., Di Giovambattista, R., 2024. Investigating the Role of Fluids in the Source Parameters of the 2013–2014 Mw 5 Matese Seismic Sequence, Southern Italy. Seismol. Res. Lett. 95 (1), 299–319.

Calderoni, G., Rovelli, A., Di Giovambattista, R., 2019. Stress drop, apparent stress, and radiation efficiency of clustered earthquakes in the nucleation volume of the 6 April 2009, Mw 6.1 L'Aquila earthquake. J. Geophys. Res.: Solid Earth 124 (10), 10360–10375.

Cao, A., Liu, Y., Jiang, S., Hao, Q., Peng, Y., Bai, X., Yang, X., 2021. Numerical investigation on influence of two combined faults and its structure features on rock burst mechanism. Minerals 11 (12), 1438.

Caputa, A., Rudziński, Ł., Cesca, S., 2021. How to assess the moment tensor inversion resolution for mining induced seismicity: a case study for the Rudna Mine, Poland. Front. Earth Sci. 9, 671207.

Cesca, S., Heimann, S., Kriegerowski, M., Saul, J., Dahm, T., 2017. Moment tensor inversion for nuclear explosions: What can we learn from the 6 January and 9 September 2016 nuclear tests, North Korea? Seismol. Res. Lett. 88 (2A), 300–310.

Cesca, S., Rohr, A., Dahm, T., 2013. Discrimination of induced seismicity by full moment tensor inversion and decomposition. J. Seismol. 17, 147–163.

Chen, D., Wang, E.Y., Li, N., 2021. Study on the source parameters of the micro-earthquakes in Laohutai coal mine based on double difference relocation. Soil Dyn. Earthq. Eng. 142, 106540.

Dahm, T., Becker, D., Bischoff, M., Cesca, S., Dost, B., Fritschen, R., Hainzl, S., Klose, C.D., Kühn, D., Lasocki, S., Meier, T., 2013. Recommendation for the discrimination of human-related and natural seismicity. J. Seismol. 17, 197–202.

Dahm, T., Krüger, F., 2014. Moment tensor inversion and moment tensor interpretation. In: Bormann, P. (Ed.), New Manual of Seismological Observatory Practice 2 (NMSOP-2), Potsdam: Deutsches GeoForschungsZentrum GFZ, pp. 1–37.

De Santis, F., Contrucci, I., Kinscher, J., Bernard, P., Renaud, V., Gunzburger, Y., 2019. Impact of geological heterogeneities on induced-seismicity in a deep sublevel stoping mine. Pure Appl. Geophys. 176, 697–717.

Donnelly, L.J., Rees, J.G., 2001. Tectonic and mining induced fault reactivation around Barlaston on the Midlands Microcraton, North Staffordshire, UK. Q. J. Eng. Geol. Hydrogeol. 34 (2), 195–214.

Dost, B., van Stiphout, A., Kühn, D., Kortekaas, M., Ruigrok, E., Heimann, S., 2020. Probabilistic moment tensor inversion for hydrocarbon-induced seismicity in the Groningen gas field, the Netherlands, part 2: Application. Bull. Seismol. Soc. Am. 110 (5), 2112–2123.

Dreger, D.S., Ford, S.R., Walter, W.R., 2008. Source analysis of the Crandall Canyon, Utah, mine collapse. Science 321 (5886), 217–217.

Ford, S.R., Dreger, D.S., Walter, W.R., 2008. Source characterisation of the 6 August 2007 Crandall Canyon Mine seismic event in central Utah. Seismol. Res. Lett. 79 (5), 637–644.

Geiger, L., 1912. Probability method for the determination of earthquake epicentres from the arrival time only. Bull. St. Louis Univ. 8, 60.

Gibowicz, S.J., 2009. Seismicity induced by mining: Recent research. Adv. Geophys. 51, 1–53.

Gudmundsson, M.T., Jónsdóttir, K., Hooper, A., Holohan, E.P., Halldórsson, S.A., Ófeigsson, B.G., Cesca, S., Vogfjörd, K.S., Sigmundsson, F., Högnadóttir, T., Einarsson, P., 2016. Gradual caldera collapse at Bárdarbunga volcano, Iceland, regulated by lateral magma outflow. Science 353 (6296), https://doi.org/10.1126/science.aaf8988.

Hanks, T.C., Kanamori, H., 1979. A moment magnitude scale. J. Geophys. Res.: Solid Earth 84 (B5), 2348–2350.

Heesakkers, V., Murphy, S., Reches, Z., 2011. Earthquake rupture at focal depth, Part I: Structure and rupture of the Pretorius fault, TauTona mine, South Africa. Pure Appl. Geophys. 168, 2395–2425.

Heimann, S., Isken, M., Kühn, D., Sudhaus, H., Steinberg, A., Vasyura-Bathke, H., Daout, S., Cesca, S., Dahm, T., 2018. Grond - A probabilistic earthquake source inversion framework. V. 1.0. GFZ Data Services. https://doi.org/10.5880/GFZ.2.1.2018.003.

Heimann, S., Kriegerowski, M., Isken, M., Cesca, S., Daout, S., Grigoli, F., Juretzek, C., Megies, T., Nooshiri, N., Steinberg, A., Sudhaus, H., Vasyura-Bathke, H., Willey, T., Dahm, T., 2017. Pyrocko-An open-source seismology toolbox and library. V. 0.3. GFZ Data Services. https://doi.org/10.5880/GFZ.2.1.2017.001.

Heimann, S., Vasyura-Bathke, H., Sudhaus, H., Isken, M.P., Kriegerowski, M., Steinberg, A., Dahm, T., 2019. A Python framework for efficient use of precomputed Green's functions in seismological and other physical forward and inverse source problems. Solid Earth 10 (6), 1921–1935.

Jiang, B., Wang, L., Lu, Y., Wang, C., Ma, D., 2016. Combined early warning method for rockburst in a Deep Island, fully mechanised caving face. Arab. J. Geosci. 9, 743.

Jiang, B., Wu, K., Wang, Q., Kang, H., Zhang, B., Zhang, Z., Chen, C., 2024. Development of physical model test system for fault-slip induced rockburst in underground coal mining. J. Rock Mech. Geotech. Eng. (in press).

Jining Energy, 2017. The 3306 working face of Yangcheng Coal Power has successfully implemented a new directional opening construction, marking a significant technological advancement. https://www.jiningcoal.com/news/subsidiary/201706/09_12392.html. (Accessed 9 June 2017).

Jost, M.U., Herrmann, R.B., 1989. A student's guide to and review of moment tensors. Seismol. Res. Lett. 60 (2), 37–57.

Kagan, Y.Y., 1991. 3-D rotation of double-couple earthquake sources. Geophys. J. Int. 106 (3), 709–716.

Kang, Q., He, F., Yin, S., Yang, Y., 2022. Attenuation law of concentrated stress under coal pillar of close coal seams and its application. Sci. Rep. 12 (1), 21753.

Kühn, D., Heimann, S., Isken, M.P., Ruigrok, E., Dost, B., 2020. Probabilistic moment tensor inversion for hydrocarbon-induced seismicity in the Groningen gas field, The Netherlands, Part 1: Testing. Bull. Seismol. Soc. Am. 110 (5), 2095–2111.

Kwiatek, G., Martínez-Garzón, P., Bohnhoff, M., 2016. HybridMT: A MATLAB/shell environment package for seismic moment tensor inversion and refinement. Seismol. Res. Lett. 87 (4), 964–976.

Linzer, L.M., 2005. A relative moment tensor inversion technique applied to seismicity induced by mining. Rock Mech. Rock Engng. 38 (2). 81–104.

Linzer, L.M., Hildyard, M.W., Wesseloo, J., 2021. Complexities of underground mining seismic sources. Phil. Trans. R. Soc. A 379 (2196), 20200134.

Lizurek, G., Rudziński, Ł., Plesiewicz, B., 2015. Mining induced seismic event on an inactive fault. Acta Geophys. 63, 176–200.

Ma, J., Dong, L., Zhao, G., Li, X., 2019. Focal mechanism of mining-induced seismicity in fault zones: a case study of yongshaba mine in China. Rock Mech. Rock Eng. 52, 3341–3352.

Madariaga, R., 1976. Dynamics of an expanding circular fault. Bull. Seismol. Soc. Am. 66 (3), 639–666.

Masethe, R.T., Manzi, M.S., Durrheim, R.J., 2023. Using legacy 3D seismic data and source parameters of mining-induced earthquakes to mitigate the risk of rockbursting in Kloof Gold Mine, South Africa. Geophys. Prospect. 71 (7), 1281–1311.

Maxwell, S.C., Chorney, D., Goodfellow, S.D., 2015. Microseismic geomechanics of hydraulic-fracture networks: Insights into mechanisms of microseismic sources. Lead. Edge 34 (8), 904–910.

McGarr, A., 1992. An implosive component in the seismic moment tensor of a mining-induced tremor. Geophys. Res. Lett. 19 (15), 1579–1582.

McGarr, A., Simpson, D., 1997. Keynote lecture: A broad look at induced and triggered seismicity, "Rockbursts and Seismicity in Mines". In: Gibowitz, S.J., Lasocki, S. (Eds.), Proceedings of 4th International Symposium on Rockbursts and Seismicity in Mines, Poland, 11–14 August 1997, A. A. Balkema Press, Rotterdam, Netherlands, pp. 385–396.

Naoi, M., Imakita, K., Chen, Y., Yamamoto, K., Tanaka, R., Kawakata, H., Ishida, T., Fukuyama, E., Arima, Y., 2022. Source parameter estimation of acoustic emissions induced by hydraulic fracturing in the laboratory. Geophys. J. Int. 231 (1), 408–425.

Ohnaka, M., 1992. Earthquake source nucleation: a physical model for short-term precursors. Tectonophysics 211 (1-4), 149–178.

Ortlepp, W.D., 2000. Observation of mining-induced faults in an intact rock mass at depth. Int. J. Rock Mech. Min. Sci. 37 (1-2), 423–436.

Paap, B., Kraaijpoel, D., Bakker, M., Gharti, H.N., 2018. Wave propagation modelling of induced earthquakes at the Groningen gas production site. Geophys. J. Int. 214 (3), 1947–1960.

Pasyanos, M.E., Ichinose, G.A., Ford, S.R., 2023. Moment tensor event identification for collapses. Geophys. J. Int. 235 (1), 635–643.

Petersen, G.M., Cesca, S., Heimann, S., Niemz, P., Dahm, T., Kühn, D., Kummerow, J., Plenefisch, T., 2021. Regional centroid moment tensor inversion of small to moderate earthquakes in the Alps using the dense AlpArray seismic network: challenges and seismotectonic insights. Solid Earth, 12 (6), 1233–1257.

Rigby, A., 2024. Physically motivated moment-tensor decomposition for mining-induced seismicity. Geophys. J. Int. 236 (1), 443–455.

Rudziński, Ł., Cesca, S., Lizurek, G., 2016. Complex rupture process of the 19 March 2013, Rudna Mine (Poland) induced seismic event and collapse in the light of local and regional moment tensor inversion. Seismol. Res. Lett. 87 (2A), 274–284.

Rudziński, Ł., Mirek, J., Lizurek, G., 2017. Identification of seismic doublets occurred on Rudna mine, Poland. Acta Geophys. 65, 287–298.

Song, C.H., Lu, C.P., Liu, H.Q., Song, J.F., Liu, C.Y., Cui, H.W., Zhang, J.R., 2024. Moment Tensor and Stress Field Inversions of Mining-Induced Seismicity in A Thick-Hard Roof Zone. Rock Mech. Rock Eng. 57 (3), 2267–2287.

Song, C.H., Lu, C.P., Zhang, X.F., Wang, C., Xie, H.D., Yan, X.Y., Yang, H.W., 2022. Moment tensor inversion and stress evolution of coal pillar failure mechanism. Rock Mech. Rock Eng. 55 (4), 2371–2383.

Song, C.H., Lu, C.P., Zhang, X.F., Wang, Y.Q., Song, J.F., Liu, Y., 2023. Moment tensor inversion and coseismic stress characteristics of mining-induced seismicity in coal pillar area. Rock Mech. Rock Eng. 56 (9), 6285–6298.

Song, J.F., Lu, C.P., Zhang, X.F., Song, C.H., Zhou, J., Zhang, Z.G., 2024. Application of Bayesian method for mining-induced tremors: A case study of the Xinjulong coal mine in China. Int. J. Rock Mech. Min. Sci. 174, 105635.

Sprenke, K.F., White, B.G., Rohay, A.C., Whyatt, J.K., Stickney, M.C., 2002. Comparison of body-wave displacement with damage observations of a Rockburst, Coeur d'Alene Mining District, Idaho. Bull. Seismol. Soc. Am. 92 (8), 3321–3328.

Stec, K., 2007. Characteristics of seismic activity of the Upper Silesian Coal Basin in Poland. Geophys. J. Int. 168 (2), 757–768.

Stork, A.L., Verdon, J.P., Kendall, J.M., 2014. The robustness of seismic moment and magnitudes estimated using spectral analysis. Geophys. Prospect. 62 (4), 862–878.

Talebi, S., Côté, M., 2005. Implosional focal mechanisms in a hard-rock mine. In Controlling Seismic Risk, RaSiM6: Proceedings of the Sixth International Symposium on Rockburst and Seismicity in Mines Proceedings, Y. Potvin, and M. Hudyma (Eds.), Nedlands, Australia, pp. 113–121.

Tape, W., Tape, C., 2012a. A geometric setting for moment tensors. Geophys. J. Int. 190 (1), 476–498.

Tape, W., Tape, C., 2012b. A geometric comparison of source-type plots for moment tensors. Geophys. J. Int. 190 (1), 499–510.

Verdon, J.P., Kendall, J.M., Butcher, A., Luckett, R., Baptie, BJ, 2018. Seismicity induced by longwall coal mining at the Thoresby Colliery, Nottinghamshire, UK. Geophys. J. Int. 212 (2), 942–954.

Wang, H., Shi, R., Lu, C., Jiang, Y., Deng, D., Zhang, D., 2019. Investigation of sudden faults instability induced by coal mining. Saf. Sci. 115, 256–264.

Wang, R., 1999. A simple orthonormalisation method for stable and efficient computation of Green's functions. Bull. Seismol. Soc. Am. 89 (3), 733–741.

Whyatt, J., Blake, W., Williams, T., White, B., 2002. 60 years of rockbursting in the Coeur d'Alene District of Northern Idaho, USA: lessons learned and remaining issues. In: Proceedings of the 2002 SME Annual Meeting and Exhibit. Phoenix: Society for Mining, Metallurgy, and Exploration, Inc., Arizona, USA, pp. 1–10.

Wuestefeld, A., Kendall, J.M., Verdon, J.P., Van As, A., 2011. In situ monitoring of rock fracturing using shear wave splitting analysis: an example from a mining setting. Geophys. J. Int. 187 (2), 848–860.

Yabe, Y., Nakatani, M., Naoi, M., Philipp, J., Janssen, C., Watanabe, T., Katsura, T., Kawakata, H., Georg, D., Ogasawara, H., 2015. Nucleation process of an M2 earthquake in a deep gold mine in South Africa inferred from on-fault foreshock activity. J. Geophys. Res.: Solid Earth 120 (8), 5574–5594.

Yamada, T., Mori, J.J., Ide, S., Abercrombie, R.E., Kawakata, H., Nakatani, M., Iio, Y., Ogasawara, H., 2007. Stress drops and radiated seismic energies of microearthquakes in a South African gold mine. J. Geophys. Res.: Solid Earth 112 (B3), https://doi.org/10.1029/2006JB004553.

Zhao, Y., Wang, H., Liu, S., Mu, Z., Lu, Z., 2018. Dynamic failure risk of coal pillar formed by irregular shape longwall face: a case study. Int. J. Min. Sci. Technol. 28 (5), 775–781.

Chunhui Song is a doctoral candidate in Mining Engineering at the School of Mines, China University of Mining and Technology. His current research includes seismic moment tensor inversion and travel-time tomography.

Declaration of interests

☒ The authors declare that they have no known competing financial interests or personal relationships that could have appeared to influence the work reported in this paper.

☐The authors declare the following financial interests/personal relationships which may be considered as potential competing interests: